PHYSICAL REVIEW E **86**, 041504 (2012)

Relationship between bond-breakage correlations and four-point correlations in heterogeneous glassy dynamics: Configuration changes and vibration modes

Hayato Shiba,[1,*] Takeshi Kawasaki,[2,*] and Akira Onuki[2]
[1]*Institute for Solid State Physics, University of Tokyo, Chiba 277-8581, Japan*
[2]*Department of Physics, Kyoto University, Kyoto 606-8502, Japan*

(Received 28 May 2012; published 10 October 2012; corrected 24 October 2012)

We investigate the dynamic heterogeneities of glassy particle systems in the theoretical schemes of bond breakage and four-point correlation functions. In the bond-breakage scheme, we introduce the structure factor $S_b(q,t)$ and the susceptibility $\chi_b(t)$ to detect the spatial correlations of configuration changes. Here $\chi_b(t)$ attains a maximum at $t = t_b^{\max}$ as a function of time t, where the fraction of the particles with broken bonds $\phi_b(t)$ is about 1/2. In the four-point scheme, treating the structure factor $S_4(q,t)$ and the susceptibility $\chi_4(t)$, we detect superpositions of the heterogeneity of bond breakage and that of thermal low-frequency vibration modes. While the former grows slowly, the latter emerges quickly to exhibit complex space-time behavior. In two dimensions, the vibration modes extending over the system yield significant contributions to the four-point correlations, which depend on the system size logarithmically. A maximum of $\chi_4(t)$ is attained at $t = t_4^{\max}$, where these two contributions become of the same order. As a result, $t_4^{\max}$ is considerably shorter than $t_b^{\max}$.

DOI: 10.1103/PhysRevE.86.041504 PACS number(s): 64.70.Q−, 63.50.Lm, 61.20.Lc, 66.30.hh

I. INTRODUCTION

Recently, much attention has been paid to the dynamics of glasses [1]. In particular, dynamic heterogeneities exceeding the molecular size and emerging on long time scales [2] have been observed in a number of experiments [3–5] and molecular dynamics simulations in two dimensions (2D) and in three dimensions (3D) [5–21]. In simulations, they can be detected if the spatial correlations of the particle configuration changes or the displacements between two separated times are calculated. In an early period, displacement heterogeneities were observed in applied strain in model amorphous alloys [6–8]. Harrowell and co-workers visualized them in a one-component fluid [9] and a binary mixture [10]. Muranaka and Hiwatari detected them on short [11] and long [12] time scales in binary mixtures. Yamamoto and one of the present authors [13,14,22] examined breakage of appropriately defined bonds and identified relatively active and inactive regions without and with applied shear flow. The bond-breakage events are produced by the configuration changes of the particle positions. The broken bonds accumulated in long time intervals are heterogeneous such that their structure factor $S_b(q,t)$ may be fitted to the Ornstein-Zernike form ($\propto 1/[1 + q^2\xi_b(t)^2]$), where t is the interval width taken to be of the order of the structural relaxation time τ_α. The correlation length $\xi_b(t)$ grows with lowering the temperature T. Kob *et al.* [15] detected stringlike motions of mobile particles as fundamental elements of structural relaxations, whose length distribution is widened with lowering T.

Lačević *et al.* [23] presented a statistical theory of the dynamic heterogeneity in terms of the so-called four-point dynamic correlation functions. They found that the four-point structure factor $S_4(q,t)$ can be fitted to the Ornstein-Zernike form and the susceptibility $\chi_4(t)$ exhibits a peak at a characteristic time $t_4^{\max}$ of order τ_α. The correlation length $\xi_4 = \xi_4(t_4^{\max})$ thus obtained grows with lowering T. Subsequently, intensive efforts have been made to construct statistical theories and/or add further numerical results on the four-point correlations [5,24–30].

However, there has been no systematic comparison between the bond-breakage scheme and the four-point scheme. The bond-breakage events occur as rare activation processes, resulting in structural relaxations, in the absence of applied shear. In contrast, the physical processes giving rise to the four-point correlations have not yet been well understood. In this paper, we show that the four-point correlations originate twofold from the configuration changes yielding the bond-breakage correlations and from the collective particle motions arising from the low-frequency transverse vibration modes [31–41]. The time scales of these two kinds of motions are dramatically different. In the latter, clusters of relatively mobile particles carry a large fraction of the vibrational energy and are distributed throughout the system [36]. The vibration modes have been studied to explain the low-temperature thermodynamic properties of glasses [1].

In the low-frequency vibrational motions, the oscillatory particle displacements are highly heterogeneous so that the configuration changes should occur preferentially in more active regions with larger displacements, as pointed out by Schober *et al.* [33]. This structural relaxation mechanism was confirmed numerically in systems with particle numbers of about 1000 [38,39] and experimentally in quasi-two-dimensional colloidal glasses [42]. Thus, it explains the inseparable coupling between the structural disorder and the slow dynamics in glass. We mention some simulations related to this coupling. Vollmayr-Lee *et al.* [43] found in 3D that mobile particles (in their definition) are surrounded by fewer neighbors than the others. Widmer-Cooper and Harrowell [44] detected a correlation between the short-time heterogeneity in a local Debye-Waller factor and the long-time heterogeneity in 2D. Kawasaki *et al.* [21] claimed that medium-range crystalline order remaining in glass controls ease of vitrification and nature of the glass transition. In polycrystal with small grains, the relation between the structure and the slow

---

[*] These two authors contributed equally to this work.

dynamics is more understandable, where the particles at the grain boundaries initiate configuration changes [45–47].

As a closely related effect, a very small applied strain produces strongly nonaffine particle displacements in glass, indicating highly heterogeneous elastic moduli [6–8,48,49]. Naturally, the particles in such elastically softer regions exhibit larger-amplitude displacements in the thermally excited vibration modes. Tanguy *et al.* [35] showed that the classical elasticity theory holds only on spatial scales longer than a characteristic length (∼30 molecular sizes in their 2D model system). Moreover, in glass, irreversible plastic events are induced even by very small stains [14,48] and plastic deformations are highly heterogeneous often leading to shear bands [5,47,50]. Under a fixed small strain at $T = 0$ in 2D, Manning and Liu [51] numerically examined the relation between the low-frequency vibration modes and structural soft spots where configuration changes (particle rearrangements in their paper) are initiated.

The organization of this paper is as follows. In Sec. II, our simulation method will be explained. In Sec. III, the bond-breakage scheme [13,14] will be generalized. In Sec. IV, we will reexamine the four-point scheme [23], where the collective particle motions arising from the vibration modes will be identified. In Sec. V, the dynamic heterogeneities detected by these two schemes will be compared. In Sec. VI, 3D results will be presented.

II. NUMERICAL METHOD

To illustrate consequences of the bond-breakage and four-point theories, we will show the results of molecular dynamics simulation of 50 : 50 binary mixtures composed of two species, 1 and 2, in 2D and 3D in amorphous states at low temperatures. We imposed the periodic boundary condition without applying shear flow. The particle numbers of the two species are $N_1 = N_2 = N/2$. In 2D, N will be mostly 4000 or 64 000, but data for $N = 16\,000$ and 256 000 will also be given in Figs. 3 and 8. In 3D, results for $N = 10\,000$ will be presented in Sec. VI. The two species have different diameters σ_1 and σ_2 with $\sigma_2/\sigma_1 = 1.4$ in 2D and $\sigma_2/\sigma_1 = 1.2$ in 3D. The particles interact via the soft-core potential,

$$v_{\alpha\beta}(r) = \epsilon\left(\frac{\sigma_{\alpha\beta}}{r}\right)^{12} - C_{\alpha\beta} \quad (r < r_{\rm cut}), \tag{2.1}$$

where α and β represent the particle species ($\alpha,\beta = 1,2$), r is the particle distance, and ϵ is the characteristic interaction energy. The interaction lengths are defined by

$$\sigma_{\alpha\beta} = (\sigma_\alpha + \sigma_\beta)/2. \tag{2.2}$$

The potential vanishes for $r > r_{\rm cut}$, where $r_{\rm cut} = 4.5\sigma_1$ in 2D and $r_{\rm cut} = 3\sigma_1$ in 3D. The constants $C_{\alpha\beta}$ ensure the continuity of the potential at $r = r_{\rm cut}$. The masses of the two species satisfy $m_2/m_1 = (\sigma_2/\sigma_1)^d$, where d is the spatial dimensionality. The average number density is $n = N/V = 0.811\sigma_1^{-2}$ in 2D and $0.8\sigma_1^{-3}$ in 3D, where V is the system volume. The system length L is $70.2\sigma_1$ for $N = 4000$ and $281\sigma_1$ for $N = 64\,000$ in 2D, while $L = 23.2\sigma_1$ in 3D. Space and time will be measured in units of σ_1 and

$$\tau_0 = \sigma_1\sqrt{m_1/\epsilon}. \tag{2.3}$$

The temperature T will be measured in units of ϵ/k_B.

We started from a liquid state at a high temperature, quenched the system to the final low temperature, and waited for a long time of order 10^5. We imposed a thermostat in these steps. However, after this preparation of the initial states, we removed the artificial thermostat and integrated the Newton equations under the periodic boundary condition in the time range $t > 0$. This is needed to describe the effect of the vibration modes on long time scales. [See item (3) in the summary section for more discussions on the heat bath effect.] Thus, the total particle number N, the total volume V, and the total energy E are fixed in our simulation.

III. BOND-BREAKAGE THEORY

A. Background

We regard two particles i and j with positions $\boldsymbol{r}_i(t)$ and $\boldsymbol{r}_j(t)$ to be bonded if [13,14]

$$r_{ij}(t) < A_1\sigma_{\alpha\beta}, \tag{3.1}$$

where $i \in \alpha$ and $j \in \beta$. Hereafter $r_{ij}(t) = |\boldsymbol{r}_i(t) - \boldsymbol{r}_j(t)|$ is the distance between these particles at time t. At a later time $t + \Delta t$, this bond is treated to be broken if

$$r_{ij}(t + \Delta t) > A_2\sigma_{\alpha\beta}. \tag{3.2}$$

We assume that $A_1\sigma_{\alpha\beta}$ is slightly larger than the peak distance of the pair correlation functions $g_{\alpha\beta}(r)$ and A_2 is somewhat larger than A_1. In this paper, we set $A_1 = 1.15$ and $A_2 = 1.5$ in 2D and $A_1 = 1.3$ and $A_2 = 1.7$ in 3D.

Let us consider the bonds at $t = t_0$ and denote their total number as $N_b(t_0)$. A fraction of them will be broken subsequently and the total number of the remaining bonds $N_b(t_0 + \Delta t)$ at $t = t_0 + \Delta t$ decays as

$$N_b(t_0 + \Delta t)/N_b(t_0) = F_b(\Delta t). \tag{3.3}$$

For large systems, the relaxation function $F_b(\Delta t)$ may be treated to depend only on the time difference Δt (being nearly independent of the initial time t_0 for large N). It decreases with increasing Δt, so the bond-breakage time τ_b may be defined by

$$F_b(\tau_b) = e^{-1}. \tag{3.4}$$

On the other hand, the self part of the density time-correlation function is expressed as

$$F_s(q,t) = \frac{1}{N}\left\langle \sum_j \exp[i\boldsymbol{q}\cdot\Delta\boldsymbol{r}_j(t_0,t_0 + t)]\right\rangle, \tag{3.5}$$

where $\Delta\boldsymbol{r}_j(t_0,t_1) = \boldsymbol{r}_j(t_1) - \boldsymbol{r}_j(t_0)$ is the displacement vector of particle j and $\boldsymbol{q}$ is the wave vector. In Eq. (3.5), the average is taken over all the particles. In our simulation, the average over the initial time t_0 and that over a number of runs were also taken. The structural relaxation time τ_α is usually defined at $q = 2\pi$ by

$$F_s(q,\tau_\alpha) = e^{-1}. \tag{3.6}$$

Wave numbers will be measured in units of σ_1^{-1}.

In the upper panel of Fig. 1, we display $F_b(t)$ and $F_s(q,t)$ at $q = 2\pi$ for $T = 0.56$ and $N = 4000$, where $\tau_\alpha = 8.4 \times 10^3$ and $\tau_b = 2.0 \times 10^5 \cong 35\tau_\alpha$. In the previous paper [14], the relation $\tau_b \cong 10\tau_\alpha$ was found for binary mixtures with the

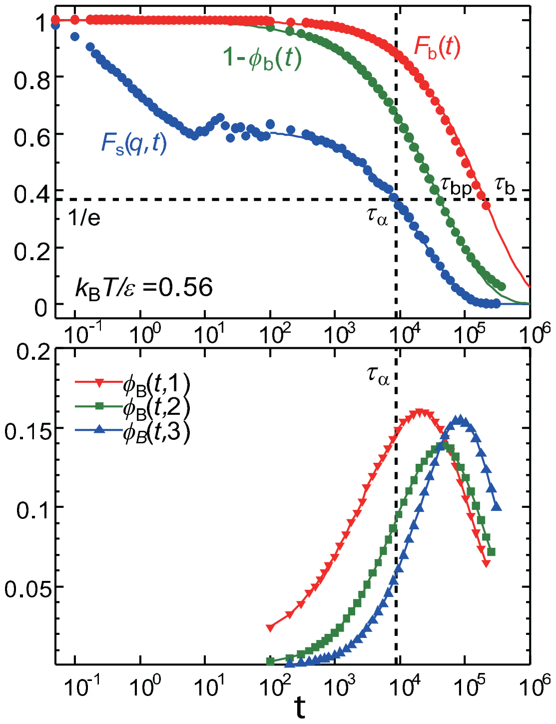

FIG. 1. (Color online) Top: Bond relaxation function $F_b(t)$ in Eq. (3.3), self part of density time-correlation function $F_s(q,t)$ at $q = 2\pi$ in Eq. (3.5), and fraction of non-***B*** particles $1-\phi_b(t) = \phi_B(t,0)$ in Eq. (3.15) at $T = 0.56$ for $N = 4000$ in 2D. Relaxation times here are $\tau_\alpha = 8400$ from Eq. (3.6), $\tau_b = 2.0\times 10^5 \cong 35\tau_\alpha$ from Eq. (3.4), and $\tau_{bp} = 4.18\times 10^4 \cong 5\tau_\alpha$ from Eq. (3.16). Bottom: fractions of ***B*** particles with k broken bonds $\phi_B(t,k)$ in Eq. (3.14) for $k = 1$, 2, and 3.

soft-core potential for $\tau_\alpha < 10^4$ wih $N = 10^4$ in 3D. Both in 2D and 3D, $F_b(t)$ may fairly be fitted to the stretched exponential form at low T as

$$F_b(t) \cong \exp[-(t/\tau_b)^c], \tag{3.7}$$

in the range $t \lesssim \tau_b$. At $T = 0.56$ we obtain $c \sim 0.58$ in 2D. The exponent c increases with decreasing T. In contrast, $F_s(q,t)$ exhibits a plateau $f_p(<1)$ before the α relaxation at low T due to the thermal vibrational motions (see the Appendix).

B. Bond-breakage correlations

Here, we present a generalized formulation of the bond breakage to introduce broken-bond correlation functions. To this end, we define two overlap functions $w^{(1)}_{\alpha\beta}(r)$ and $w^{(2)}_{\alpha\beta}(r)$ depending on the particle distance r as

$$w^{(K)}_{\alpha\beta}(r) = \theta(A_K\sigma_{\alpha\beta} - r), \tag{3.8}$$

with A_1 and A_2 being defined in Eqs. (3.1) and (3.2). The $\theta(u)$ is the step function being equal to 1 for $u > 0$ and to 0 for $u \leqslant 0$. The fluctuating number density of the bonds may then be defined as

$$\hat{n}_b(\boldsymbol{r},t) = \frac{1}{2}\sum_{ij} w^{(1)}_{\alpha\beta}[r_{ij}(t)]\delta[\boldsymbol{r} - \boldsymbol{r}_i(t)], \tag{3.9}$$

where we multiply 1/2 because a bond is supported by two particles in our definition. The statistical average of $\hat{n}_b(\boldsymbol{r},t)$ is the average bond number density,

$$n_b = \frac{1}{V}\int d\boldsymbol{r}\, \hat{n}_b(\boldsymbol{r},t) = \frac{1}{V}N_b(0). \tag{3.10}$$

Here, $n_b \sim 3n$ in 2D at high densities. In fact, we numerically obtain $n_b = 2.28 = 2.81n$ for $n = 0.811$ in our 2D system. Now we may introduce the broken-bond number density in time interval $[t_0,t_1]$ as

$$\hat{\mathcal{P}}(\boldsymbol{r},t_0,t_1) = \frac{1}{2}\sum_i \mathcal{B}_i(t_0,t_1)\delta\,[\boldsymbol{r} - \boldsymbol{r}_i(t_0)], \tag{3.11}$$

where $\mathcal{B}_i(t_0,t_1)$ is the broken-bond number of particle i assuming a non-negative integer quantity as

$$\mathcal{B}_i(t_0,t_1) = \sum_j w^{(1)}_{\alpha\beta}[r_{ij}(t_0)]\big\{1 - w^{(2)}_{\alpha\beta}[r_{ij}(t_1)]\big\}. \tag{3.12}$$

This number tends to zero as $t_1 \to t_0$ from $A_1 < A_2$ and increases to $1,2,\ldots$ upon bond breakage. Hereafter, the particles with $\mathcal{B}_i(t_0,t_1) \geqslant 1$ are called ***B*** particles, which are surrounded by different particle configurations at the initial and final times $t = t_0$ and t_1. On the other hand, those with $\mathcal{B}_i(t_0,t_1) = 0$ are called non-***B*** particles, which have the same surrounding configurations at $t = t_0$ and t_1. The statistical average $\langle\hat{\mathcal{P}}(\boldsymbol{r},t_0,t_1)\rangle$ depends on the time difference $t = t_1 - t_0$ as

$$p_b(t) = \frac{1}{V}\int d\boldsymbol{r}\ \hat{\mathcal{P}}(\boldsymbol{r},t_0,t_1) = n_b[1 - F_b(t)], \tag{3.13}$$

where n_b is defined by Eq. (3.10) and $F_b(t)$ by Eq. (3.6).

Let the number of the particles with $\mathcal{B}_i(t_0,t_1) = k$ be $N_B(t,k)$ $(k = 0,1,\ldots)$ with $t = t_1 - t_0$. Then,

$$\phi_B(t,k) = N_B(t,k)/N \tag{3.14}$$

is the fraction of the ***B*** particles with k broken bonds for $k \geqslant 1$, while $\phi_B(t,0) = N_B(t,0)/N$ is the fraction of the non-***B*** particles. The fraction of the total ***B*** particles is the following sum:

$$\phi_b(t) = \sum_{k\geqslant 1}\phi_B(t,k) = 1 - \phi_B(t,0). \tag{3.15}$$

We define the bond-preserving time $\tau_{\rm bp}$ as

$$1 - \phi_b(\tau_{\rm bp}) = \phi_B(\tau_{\rm bp},0) = e^{-1}. \tag{3.16}$$

The particles have a broken bond on this time scale. Since each particle has several bonds ($\sim$6 in 2D), $\tau_{\rm bp}$ is considerably shorter than the bond breakage time τ_b in Eq. (3.4). For $t \gtrsim \tau_{\rm bp}$, the structural relaxation becomes appreciable. From Eq. (3.14) we obtain

$$p_b(t) = \frac{n}{2}\sum_k k\phi_b(t,k). \tag{3.17}$$

From Eqs. (3.13) and (3.17) we find

$$2\frac{n_b}{n}[1 - F_b(t)] = \sum_k k\phi_b(t,k). \tag{3.18}$$

Setting $t = t_1 - t_0$ in steady states, we introduce the bond-breakage space-time correlation function,

$$\begin{aligned} G_b(r,t) &= \langle\hat{\mathcal{P}}(\boldsymbol{r}+\boldsymbol{r}',t_0,t_1)\hat{\mathcal{P}}(\boldsymbol{r}',t_0,t_1)\rangle \\ &= \frac{1}{4V}\Big\langle\sum_{ik}\mathcal{B}_i(t_0,t_1)\mathcal{B}_k(t_0,t_1)\delta\,[\boldsymbol{r} - \boldsymbol{r}_{ik}(t_0)]\Big\rangle, \end{aligned} \tag{3.19}$$

where $\boldsymbol{r}_{ik}(t_0) = \boldsymbol{r}_i(t_0) - \boldsymbol{r}_k(t_0)$. From Eq. (3.13) we have $G_b(r,t) \to p_b(t)^2$ for large r. The structure factor of the broken bonds is given by

$$\begin{aligned} S_b(q,t) &= \frac{1}{V}\langle|\hat{\mathcal{P}}_{\boldsymbol{q}}(t_0,t_1)|^2\rangle \\ &= \int d\boldsymbol{r}[G_b(\boldsymbol{r},t) - p_b(t)^2]e^{i\boldsymbol{q}\cdot\boldsymbol{r}}, \end{aligned} \tag{3.20}$$

where $\boldsymbol{q}$ is the wave vector, $q = |\boldsymbol{q}|$ is the wave number, and $\hat{\mathcal{P}}_{\boldsymbol{q}}(t_0,t_1) = \sum_j \mathcal{B}_j(t_0,t_1)\exp[i\boldsymbol{q}\cdot\boldsymbol{r}_i(t_0)]/2$ is the Fourier component of $\hat{\mathcal{P}}(\boldsymbol{r},t_0,t_1)$.

As in the four-point scheme [23], we introduce the susceptibility $\chi_b(t)$ to represent the overall degree of the bond-breakage correlations as follows:

$$\chi_b(t) = \frac{1}{4V}\left\langle\sum_{ik}\delta\mathcal{B}_i(t_0,t_1)\delta\mathcal{B}_k(t_0,t_1)\right\rangle, \tag{3.21}$$

in terms of the deviations $\delta\mathcal{B}_i(t_0,t_1) = \mathcal{B}_i(t_0,t_1) - 2p_b(t)/n$. Here $\langle\mathcal{B}_i\rangle = \sum_i \mathcal{B}_i/N = 2p_b/n$ from Eqs. (3.11) and (3.13). In $S_b(q,t)$ and $\chi_b(t)$, the four particle positions $\boldsymbol{r}_i(t_0)$, $\boldsymbol{r}_k(t_0)$, $\boldsymbol{r}_j(t_1)$, and $\boldsymbol{r}_\ell(t_1)$ are involved. In this sense, they are four-point correlation functions.

Rabini *et al.* [52] introduced the number of particles that have left particle i's original neighbors at time t. It involves two times and was written as $n_i^{\text{out}}(0,t)$. It is similar to our $\mathcal{B}_i(t_0,t_0+t)$ in Eq. (3.12). Abate and Durian [53] introduced a bond-breakage susceptibility $\chi_B(t)$ similar to ours in Eq. (3.21) for a quasi-two-dimensional granular system of air-fluidized beads.

C. Numerical results on bond breakage

We further discuss consequences of our theory using numerical results in 2D. In Fig. 1, we plot $1 - \phi_b(t) = \phi_B(t,0)$ in the upper panel and $\phi_B(t,k)$ with $k = 1$, 2, and 3 in the lower panel for $N = 4000$, where $\tau_{\text{bp}} = 41\,800 \cong 5\tau_\alpha = 0.14\tau_b$ from Eq. (3.16). At small t, $\phi_B(t,k)$ grow as

$$\phi_B(t,k) \propto t^{a_k}, \tag{3.22}$$

where $a_1 \sim 0.60$, $a_2 \sim 1.0$, and $a_3 \sim 1.3$. Though we cannot derive these exponents theoretically, they should arise from correlated occurrence of bond-breakage events.

In Fig. 2, we confirm the validity of Eq. (3.18) from simulation at $T = 0.56$, where $n_b/n = 3.17$. We find that $(2n_b/n)[1 - F_b(t)]$ nearly coincides with $\phi_B(t,1)$ for $t < 200$ and with $\phi_B(t,1) + 2\phi_B(t,2) + 3\phi_B(t,3)$ for $t < 4000$ within a few percent differences. The first relation for $k = 1$ in Eq. (3.22) is consistent with Eq. (3.18) since $a_1 \cong c$. In fact, for $t \ll \tau_b$, Eqs. (3.7) and (3.18) yield

$$\phi_B(t,1) \cong (2n_b/n)(t/\tau_b)^c. \tag{3.23}$$

In Fig. 3, we plot $\chi_b(t)$ in Eq. (3.21) as a function of t for $N = 16\,000$, which exhibits a peak at $t = t_b^{\max}$. Here, we have $\phi_b(t) \sim 0.5$ at $t = t_b^{\max}$, which can be seen in Fig. 1 for $N = 4000$ and $T = 0.56$. Here, however, $\chi_b(t)$ begins to increase for $t > t_b^{\max}$, because the $\boldsymbol{B}$ particles with $\mathcal{B}_i = 2,3,\ldots$ become appreciable at very long times (see Fig. 1). In Fig. 4(a), we show $S_b(q,t_b^{\max})$ vs q for various T with $N = 64\,000$. In its calculation we took the average over the initial time t_0 in a wide range of $[0,10^6]$ for $T \geqslant 0.64$ and that of $[0,2\times10^6]$ for $T = 0.56$, which was needed because of the slow bond breakage. We may fairly fit $S_b(q,t)$ to the Ornstein-Zernike form [13,14],

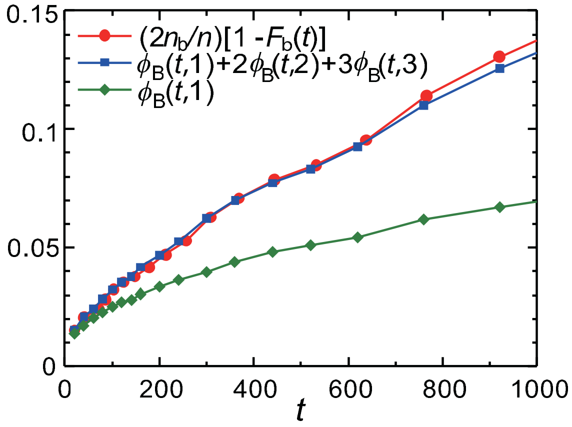

FIG. 2. (Color online) Numerical results of $(2n_b/n)[1 - F_b(t)]$, $\phi_B(t,1)$, and $\phi_B(t,1) + 2\phi_B(t,2) + 3\phi_B(t,3)$ as functions of t in the early stage at $T = 0.56$ for $N = 4000$, which confirm Eq. (3.18).

$$S_b(q,t) = \chi_b^0(t)/[1 + q^2\xi_b(t)^2], \tag{3.24}$$

where $\chi_b^0(t) = \lim_{q\to0} S_b(q,t)$ is the long-wavelength limit of $S_b(q,t)$ and $\xi_b = \xi_b(t)$ is the correlation length representing the spatial scale of the correlated configuration changes. Furthermore, in Fig. 4(b), we show $S_b(q,t_b^{\max})$ vs q at $T = 0.56$ for various N, which demonstrates weak system-size dependence of the bond-breakage correlations. For $N = 256\,000$, however, the averaging over the initial time t_0 is still insufficient because of very large $t_b^{\max} \sim 4\times10^4$ as compared to the simulation time ($\sim10^5$). As a result, the corresponding $S_b(q,t_b^{\max})$ exhibit noticeable fluctuations at small q. In (c), the correlation length ξ_b vs T is plotted at $t = t_b^{\max}$ for $N = 64\,000$, which increases with lowering T. Note that $\xi_b = \xi_b(t_b^{\max})$ is nearly independent of the system size from (b) as long as $1 \ll \xi_b \ll L$.

In the original papers [13,14], the broken-bond structure factor was defined differently, so it is written as $S_b^{\text{YO}}(q,t)$ here. It was calculated for the Fourier component of the following

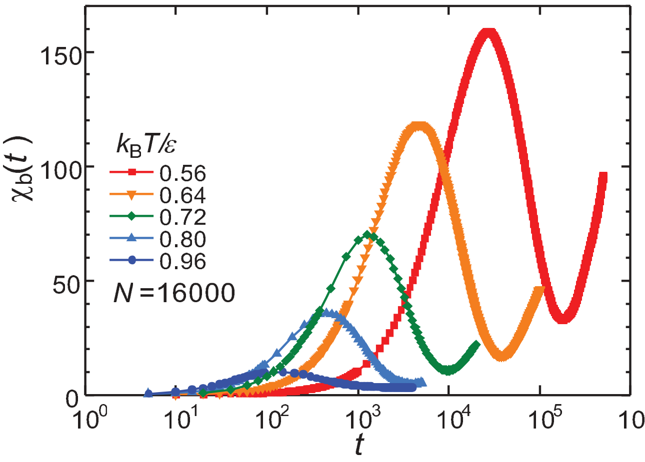

FIG. 3. (Color online) Susceptibility $\chi_b(t)$ in Eq. (3.21) vs t exhibiting a peak at $t = t_b^{\max}$ for $N = 16\,000$.

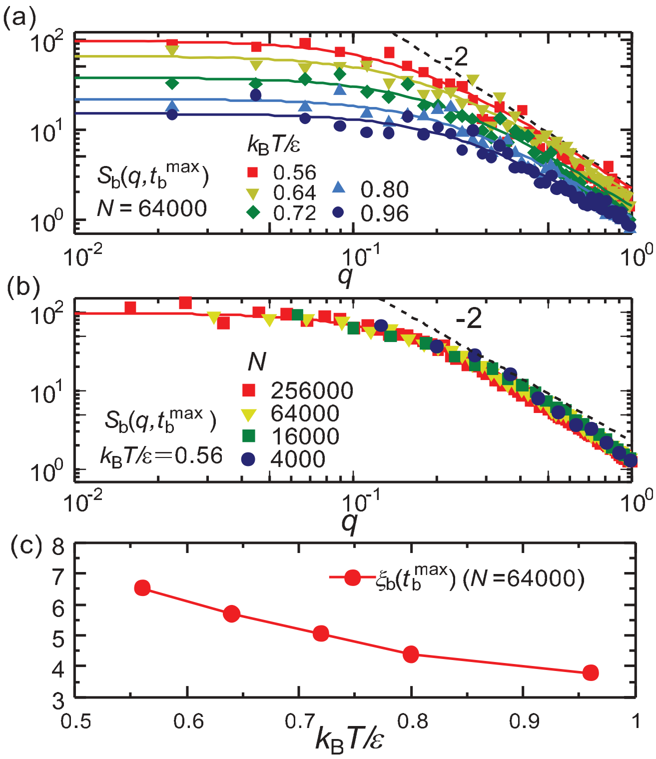

FIG. 4. (Color online) (a) Structure factor $S_b(q,t_b^{\max})$ for bond breakage in Eq. (3.20) at various T for $N = 64\,000$, (b) $S_b(q,t_b^{\max})$ at $T = 0.56$ for various N, and (c) correlation lengths $\xi_b = \xi_b(t_b^{\max})$ vs T for $N = 64\,000$. $S_b(q,t)$ is approximately on a single curve independent of N, leading to weak system-size dependence of ξ_b for $1 \ll \xi_b \ll L$.

broken-bond number density,

$$\hat{\mathcal{P}}_{\rm YO}(\boldsymbol{r},t_0,t_1) = \frac{1}{2}\sum_{ij} w^{(1)}_{\alpha\beta}[r_{ij}(t_0)]\{1 - w^{(2)}_{\alpha\beta}[r_{ij}(t_1)]\} \times \delta[\boldsymbol{r} - \boldsymbol{R}_{ij}(t_0)], \qquad (3.25)$$

where $t = t_1 - t_0$ was set equal to $0.05\tau_b$ or $0.1\tau_b$. Here, the midpoint position $\boldsymbol{R}_{ij}(t_0) = \frac{1}{2}[\boldsymbol{r}_i(t_0) + \boldsymbol{r}_j(t_0)]$ of the two particles i and j is used instead of the position $\boldsymbol{r}_i(t_0)$ in $\delta[\boldsymbol{r} - \boldsymbol{r}_i(t_0)]$ in Eq. (3.11). Note that the particle pairs with a common broken bond are included in $S_b(q,t)$. As a result, the interparticle peak at $q \cong 2\pi$ appears in $S_b(q,t)$ (which is not shown in Fig. 4), while it does not apppear in $S_b^{\rm YO}(q,t)$. However, there is no essential difference between these two definitions for $q < 2$. In addition, in the previous work [14], the dynamic scaling relation of the form $\tau_b \sim \xi_b^z$ was obtained, where $z = 4$ in 2D and $z = 2$ in 3D.

IV. FOUR-POINT THEORY

Lačević *et al.* [23] introduced the four-point correlation function to analyze the dynamic heterogeneity in glassy systems. In their numerical analysis of a 3D binary mixture in the *NVE* ensemble, they used the Lennard-Jones potential, where the particle size ratio was $\sigma_2/\sigma_1 = 1.2$ and the particle numbers were $N_1 = N_2 = 4000$. We critically review their theory comparing it with our theory of bond breakage using some numerical analysis.

A. Overlap and nonoverlap with initial regions

For a time interval $[t_0,t_1]$ $(t = t_1 - t_0 > 0)$, we introduce a fluctuating density variable,

$$\hat{Q}(\boldsymbol{r},t_0,t_1) = \sum_i \mathcal{F}_i(t_0,t_1)\delta[\boldsymbol{r} - \boldsymbol{r}_i(t_0)]. \qquad (4.1)$$

For each i we define a non-negative integer,

$$\mathcal{F}_i(t_0,t_1) = \sum_j w[|\boldsymbol{r}_i(t_0) - \boldsymbol{r}_j(t_1)|], \qquad (4.2)$$

using the following overlap function [23]:

$$w(r) = \theta(A_4\sigma_1 - r). \qquad (4.3)$$

The overlap length $A_4\sigma_1$ is common for the two particle species for simplicity. In Eq. (4.2) the particle positions $\boldsymbol{r}_i(t_0)$ and $\boldsymbol{r}_j(t_1)$ are those at different times. Thus $\mathcal{F}_i(t_0,t_1)$ is the number of overlapping particles in the initial circle (or sphere in 3D) $|\boldsymbol{r} - \boldsymbol{r}_i(t_0)| < A_4\sigma_1$ in two configurations separated by time $t = t_1 - t_0$. We may call $\hat{Q}(\boldsymbol{r},t_0,t_1)$ the two-point overlap density.

In the original analysis [23], the overlap function was written as $w(r) = \theta(a\sigma_2 - r)$ with $a\sigma_2 = 1.2a\sigma_1$, where the parameter a was set equal to 0.3 maximizing the four-point susceptibility $\chi_4(t)$ [see the discussion around Eq. (4.17) below]. In numerical analysis in this paper, we set $A_4 = 0.3$ in Eq. (4.3). These selected values are considerably shorter than the particle radii, but somewhat exceed the square root of the plateau value of the mean square displacement [23]. Thus, as $t_1 \to t_0$, the distinct terms with $j \neq i$ vanish in the summation of Eq. (4.2), leading to $\mathcal{F}_i(t_0,t_1) \to 1$ and $\hat{Q}(\boldsymbol{r},t_0,t_1) \to \hat{\rho}(\boldsymbol{r},t_0)$, where $\hat{\rho}(\boldsymbol{r},t) = \sum_i \delta[\boldsymbol{r} - \boldsymbol{r}_i(t)]$ is the usual fluctuating number density. For $t_1 > t_0$, $\mathcal{F}_i(t_0,t_1)$ is either 0 or 1. We did not detect the particles with $\mathcal{F}_i \geqslant 2$ in our simulation.

In the definition of $\hat{Q}(\boldsymbol{r},t_0,t_1)$, the terms in Eqs. (4.1) and (4.2) may be divided into the self part with $i = j$ and the distinct part with $i \neq j$. The self part of $\hat{Q}$ reads

$$\hat{Q}_s(\boldsymbol{r},t_0,t_1) = \sum_i w\,[\Delta r_i(t_0,t_1)]\,\delta\,[\boldsymbol{r} - \boldsymbol{r}_i(t_0)], \qquad (4.4)$$

where $\Delta r_i(t_0,t_1)$ is the displacement length of particle i,

$$\Delta r_i(t_0,t_1) = |\boldsymbol{r}_i(t_1) - \boldsymbol{r}_i(t_0)|. \qquad (4.5)$$

Setting $a = 0.3$, Lačević *et al.* [23] found that the self part gives rise to the dominant contributions in the four-point correlations. Also in our simulation, the self part dominates over the distinct part. We consider the particles with $\Delta r_i > 0.3$ and $\mathcal{F}_i = 1$, for which another particle j has moved within the initial circle of particle i giving rise to the distinct contribution. We compare their number with the number of the particles with $\Delta r_i > 0.3$. For example, in a 2D simulation run for $T = 0.56$ and $N = 4000$ (which yielded Fig. 13 and the left panels of Fig. 14), these numbers are 256 and 2195, respectively, at $t = 10\,200$ (see Table II). In a 3D simulation run for $T = 0.24$ and $N = 10^4$ (which yielded Figs. 15 and 16), they are 366 and 1452, respectively, at $t = 10^4$ (see Table IV). More than 90% of these distinct particles (with $\Delta r_i > 0.3$ and $\mathcal{F}_i = 1$) are $\boldsymbol{B}$ particles having broken bonds.

B. Background vibrational fluctuations

We first examine the fluctuations of the particle positions due to the thermally excited low-frequency vibration modes at low T before the onset of the structural relaxation. They exhibit significant heterogeneity, as found by Muranaka and Hiwatari in a very short time interval of width 5 in a 2D soft-core system with $N = 10^4$ [11].

For $t \ll \tau_{\rm bp}$, we may neglect the configuration changes from the discussion below Eq. (3.16) and define the displacement vector $\boldsymbol{u}_i(t) = \boldsymbol{r}_i(t) - \bar{\boldsymbol{r}}_i$, where $\bar{\boldsymbol{r}}_i$ is the time-averaged position in a time interval with width much shorter than $\tau_{\rm bp}$. The equal-time variance $\langle|\boldsymbol{u}|^2\rangle = \sum_i\langle|\boldsymbol{u}_i|^2\rangle/N$ is a half of the plateau value $M_{\rm p}$ of the mean square displacement at low T [see Eq. (A5) below]. From the Appendix, $\langle|\boldsymbol{u}|^2\rangle$ increases with increasing the system length L logarithmically in 2D as [54]

$$\langle|\boldsymbol{u}|^2\rangle = M_{\rm p}/2 \cong C_0 + C_1 \ln(L/\sigma_1), \tag{4.6}$$

where C_0 and C_1 are functions of T and are independent of L. In terms of the shear modulus μ and the bulk modulus K, the coefficient C_1 is expressed as

$$C_1 = \frac{k_B T}{2\pi}\left(\frac{1}{\mu} + \frac{1}{K+\mu}\right). \tag{4.7}$$

In our 2D system, we obtained $\mu \cong 18$ and $K \cong 67.5$ at $T = 0.56$ from the initial linear growth of the stress-strain relation and the density-pressure relation (not shown in this paper) [55]. Then we find $C_1 \cong 0.0060$ at $T = 0.56$. If the total particle number is increased from 4000 to 64 000, Eq. (4.6) yields the incremental increase $C_1 \ln 4 \cong 0.0083$ in $\langle|\boldsymbol{u}|^2\rangle$. In fair agreement with this estimate, we numerically calculated $\langle|\boldsymbol{u}|^2\rangle$ to be 0.02266 for $N = 4000$ and 0.03305 for $N = 64\,000$, where $\bar{\boldsymbol{r}}_i$ was equated with the time average of $\boldsymbol{r}_i(t)$ in a time interval of width 200.

With Eq. (4.6), we need to examine how the particles remain within or go outside their initial circle. In Fig. 5, we display $\Delta r_i(t_0,t_1)$ in Eq. (4.5) for five particles in time range $t = t_1 - t_0 < 18\,000$ with $N = 4000$. These particles are separated from one another with distances longer than 10. We recognize that these displacements undergo rapid thermal fluctuations with magnitudes nearly equal to the overlap length 0.3. In the early stage ($t < \tau_{\rm bp}$), most of $\mathcal{F}_i$ fluctuate between 1 and 0. In this example, two of them escape from their initial circle, where one has a broken bond at $t \sim 8000$ and the other has two broken bonds at $t \sim 10\,000$ (see Fig. 6). Each jump itself occurs on a short time of order 10. Figure 6(a) gives the trajectory of the particle escaping from a cage at $t \sim 10^4$ in Fig. 5. In Fig. 6(b), this escape take place as a stringlike motion involving several particles as in 3D [15,33]. See Fig. 13(a) below for other examples. In Fig. 6(b), we can see that most of the particles involved have only one broken bond, which is particularly the case for isolated configuration changes. Therefore, these motions may also be treated as small slips in 2D.

Removing the rapid temporal fluctuations, we calculated the smoothed displacement lengths,

$$\Delta\bar{r}_i(t) = |\bar{\boldsymbol{r}}_i(t+t_0) - \bar{\boldsymbol{r}}_i(t_0)|, \tag{4.8}$$

for the time-smoothed positions,

$$\bar{\boldsymbol{r}}_i(t) = \frac{1}{t_{\rm sm}}\int_0^{t_{\rm sm}} dt'\,\boldsymbol{r}_i(t+t'). \tag{4.9}$$

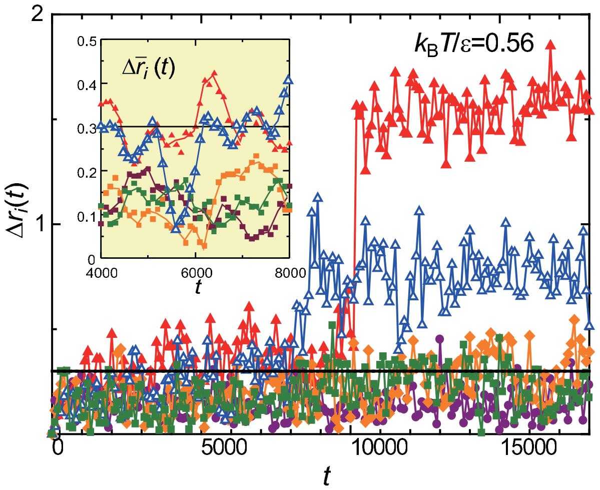

FIG. 5. (Color online) Time evolution of $\Delta r_i(t_0,t_0+t)$ for five particles among 4000 particles. They exhibit thermal fluctuations with magnitudes on the order of the overlap length 0.3. Two particles escape from the initial circle at $t \sim 8000$ (blue △) and $\sim 10^4$ (red ▲). They have a broken bond with $\mathcal{B}_i(t_0,t_0+t) = 1$ and $\mathcal{F}_i(t_0,t_0+t) = 0$ in later times. For the other three particles, the bonds are preserved, but $\mathcal{F}_i$ frequently fluctuate between 1 and 0 in the time range displayed. Inset: Time evolution of the time-smoothed distance $\Delta\bar{r}_i(t)$ defined in Eqs. (4.8) and (4.10) in the range $4000 < t < 8000$.

In the inset of Fig. 5, the smoothing time $t_{\rm sm}$ is 500. Even on this time scale, the particles move considerably, even across their initial circle. Note that this $t_{\rm sm}$ is much longer than the traversal time of the transverse sounds across the system $t_a = L/c_\perp \sim 17$ for $N = 4000$ [55]. These complex fluctuations can arise from bond breakage events close to these particles and from superposition of weakly coupled, low-frequency vibration modes [31–41].

In Fig. 7, we show the particles with $\mathcal{F}_i = 0$ at very early times $t = 200$ and 400 for $T = 0.56$ and $N = 4000$, where their initial circles contain no particle. The fraction of the particles with $\mathcal{F}_i = 0$, written as $\phi_4(t)$, is soon about 0.2 for $t \gtrsim 10$. That is, a considerable amount of the non-$\boldsymbol{B}$ particles with $\mathcal{F}_i = 0$ already appear from very early times. However, some of the $\boldsymbol{B}$ particles depicted at $t = 200$ are changed to those with $\mathcal{F}_i = 1$ at $t = 400$ (see the sentences at the end of Sec. IV A).

In Fig. 8, we show the particles with $\mathcal{F}_i = 0$ at $t = 10^4 \sim \tau_\alpha$ for $T = 0.56$ in a much larger system of $N = 64\,000$. Some heterogeneities have sizes of order 50. Among the displayed particles, the $\boldsymbol{B}$ and non-$\boldsymbol{B}$ particles amount to 22 034 and 18 122, respectively. The patterns of the latter are more extended than those of the former. Moreover, their time scales are distinctly separated (see Fig. 14 below). These indicate the presence of thermally excited large-scale vibration modes.

C. Four-point correlations

The average of $\hat{Q}(\boldsymbol{r},t_0,t_1)$ in Eq. (4.1) is written as

$$\begin{aligned} q_4(t) &= \langle\hat{Q}(\boldsymbol{r},t_0,t_1)\rangle \\ &= \frac{1}{V}\sum_{ij} w[|\boldsymbol{r}_i(t_0) - \boldsymbol{r}_j(t_1)|], \end{aligned} \tag{4.10}$$

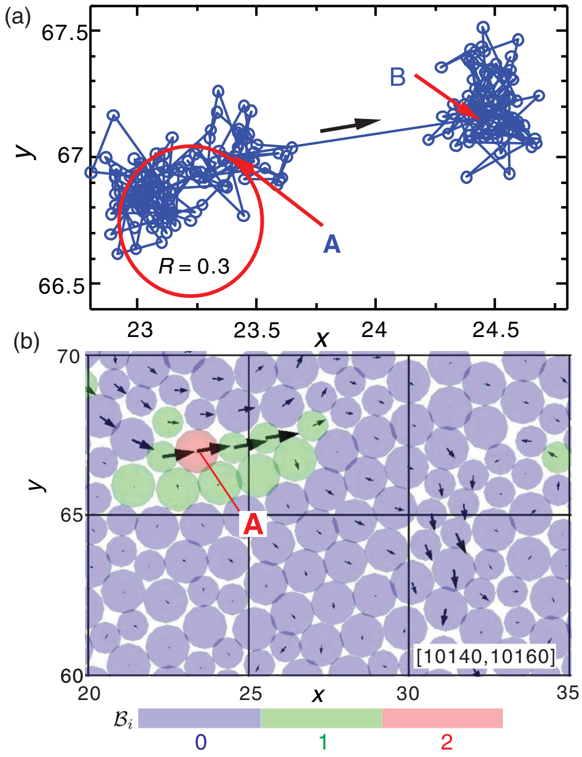

FIG. 6. (Color online) (a) Trajectory of the particle escaping from a cage (red ▲ in Fig. 5). Data points at $t = 8000 + 20k$ $(k = 0,1,\ldots,180)$ are written. Its position is $(x,y) = (23.36,67.00)$ at $t = 10\,140$ (point A) and $(x,y) = (24.44,67.16)$ at $t = 10\,160$ (point B). Between these times, the particle escapes from the circle $|\boldsymbol{r} - \boldsymbol{r}_i(t_0)| < 0.3$ (red loop line). (b) Displacements between this short time interval [10 140,10 160]. Several particles undergo a stringlike motion, where the particle (A) in the upper panel has two broken bonds and the others have one broken bond.

which is a function of $t = t_1 - t_0$. In our simulation, $\mathcal{F}_i = 1$ or 0, so $q_4(t)$ is related to the fraction $\phi_4(t)$ of the particles with $\mathcal{F}_i = 0$ as

$$q_4(t) = n[1 - \phi_4(t)]. \tag{4.11}$$

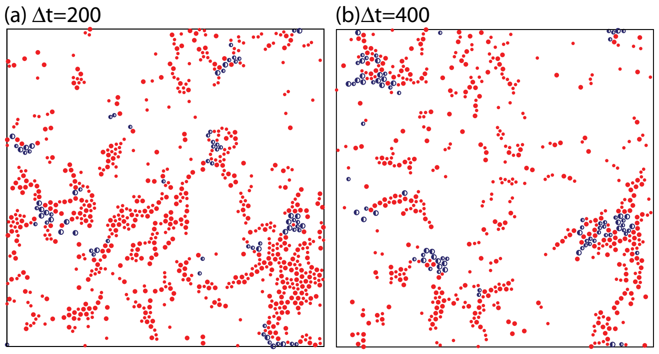
(a) Δt=200 (b)Δt=400

FIG. 7. (Color online) Early-stage snapshots of particles with $\mathcal{F}_i = 0$ at $t = 200$ (left) and 400 (right), which are classified into those with $\mathcal{B}_i = 0$ (full circle symbol in red) and those with $\mathcal{B}_i = 1$ (crescentic symbol in blue). Here $T = 0.56$ and $N = 4000$. Numbers of the former $(\mathcal{B}_i = 0)$ and the latter $(\mathcal{B}_i = 1)$ are (766,75) in (a) and (535,81) in (b). The former arise from the collective vibrational modes emerging for $t \gtrsim 10$.

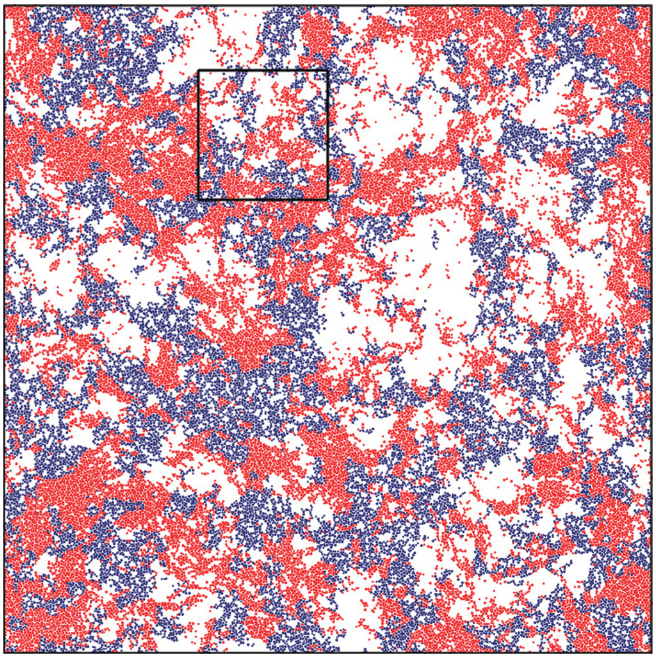

FIG. 8. (Color online) Late-stage snapshot of particles with $\mathcal{F}_i = 0$ in a large system of $N = 64\,000$ and $L = 281$, where $t = 10^4$ and $T = 0.56$. Depicted particles are classified into those with $\mathcal{B}_i = 0$ (red or lighter gray) and those with $\mathcal{B}_i \geqslant 1$ (blue or darker gray). Numbers of the former $(\mathcal{B}_i = 0)$ and the latter $(\mathcal{B}_i \geqslant 1)$ are (22 034,18 122), respectively. The former arise from the low-frequency vibration modes. Subsequent time evolution in the upper box region will be given in the right of Fig. 14.

Here, $q_4(0) = n$ and $q_4(\infty) = v_0 n^2$, where v_0 is the area or volume of the overlap region [$v_0 = \pi(A_4\sigma_1)^2$ in 2D and $v_0 = 4\pi(A_4\sigma_1)^3/3$ in 3D].

As in Eq. (3.19) for $G_b(r,t)$, the four-point space-time correlation function is given by

$$\begin{aligned} G_4(r,t) &= \langle \hat{\mathcal{Q}}(\boldsymbol{r} + \boldsymbol{r}', t_0, t_1)\hat{\mathcal{Q}}(\boldsymbol{r}', t_0, t_1)\rangle \\ &= \frac{1}{V}\left\langle \sum_{ik} \mathcal{F}_i(t_0,t_1)\mathcal{F}_k(t_0,t_1)\delta(\boldsymbol{r} - \boldsymbol{r}_{ik}(t_0))\right\rangle, \end{aligned} \tag{4.12}$$

where $\boldsymbol{r}_{ik}(t_0) = \boldsymbol{r}_i(t_0) - \boldsymbol{r}_k(t_0)$. The four-point structure factor is defined by

$$\begin{aligned} S_4(q,t) &= \frac{1}{V}\langle|\hat{\mathcal{Q}}_{\boldsymbol{q}}(t_0,t_1)|^2\rangle \\ &= \int d\boldsymbol{r}[G_4(r,t) - q_4(t)^2]e^{i\boldsymbol{q}\cdot\boldsymbol{r}}, \end{aligned} \tag{4.13}$$

where $\hat{\mathcal{Q}}_{\boldsymbol{q}}(t_0,t_1) = \sum_j \mathcal{F}_j(t_0,t_1)\exp[i\boldsymbol{q}\cdot\boldsymbol{r}_j(t_0)]$ is the Fourier component of $\hat{\mathcal{Q}}(\boldsymbol{r},t_0,t_1)$. We define the four-point susceptibility $\chi_4(t)$ by

$$\chi_4(t) = \frac{1}{V}\left\langle \sum_{ik} \delta\mathcal{F}_i(t_0,t_1)\delta\mathcal{F}_k(t_0,t_1)\right\rangle \tag{4.14}$$

in terms of the deviation $\delta\mathcal{F}_i(t_0,t_1) = \mathcal{F}_i(t_0,t_1) - q_4(t)/n$. In these correlation functions, the four particle positions $\boldsymbol{r}_i(t_0)$, $\boldsymbol{r}_k(t_0)$, $\boldsymbol{r}_j(t_1)$, and $\boldsymbol{r}_\ell(t_1)$ are involved. However, as discussed around Eq. (4.4), the self parts with $i = j$ and $k = \ell$ dominate over the distinct parts with $i \neq j$ and $k \neq \ell$ [23].

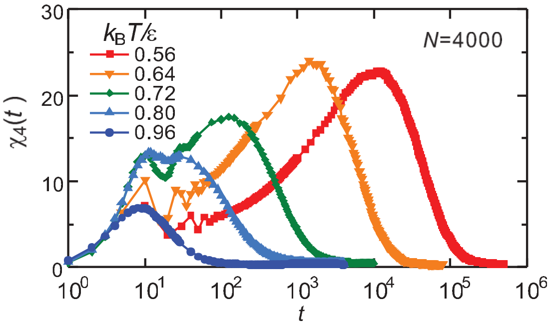

FIG. 9. (Color online) Susceptibility $\chi_4(t)$ in Eq. (4.14) vs t for $N = 4000$.

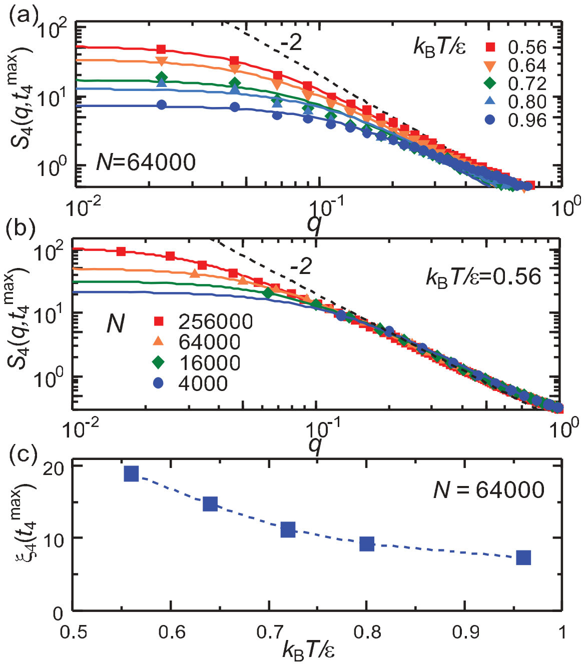

FIG. 10. (Color online) (a) Four-point structure factor $S_4(q,t_4^{\max})$ vs q in Eq. (4.13) for various T, where $N = 64\,000$. (b) $S_4(q,t_4^{\max})$ vs q for various N at $T = 0.56$. (c) $\xi_4(t_4^{\max})$ for $N = 64\,000$. Marked system-size dependence appears at small q due to the low-frequency vibration modes.

Berthier *et al.* [24,25] showed that the four-point susceptibility $\chi_4(t)$ depends on the ensemble (NVE or NVT) and the dynamics (Newtonian or Brownian). Our $\chi_4(t_4^{\max})$ in the NVE ensemble is roughly 60% of the long-wavelength limit of the four-point structure factor $\chi_4^0(t_4^{\max}) = \lim_{q\to 0} S_4(q,t_4^{\max})$, which is consistent with the previous calculations [24–28]. However, in our calculation, the long-wavelength limit of the bond-breakage structure factor $\chi_b^0(t_b^{\max}) = \lim_{q\to 0} S_b(q,t_b^{\max})$ cannot be determined reliably because of the very long $t_b^{\max}$ at low T (see Fig. 4) and our maximum bond-breakage susceptibility $\chi_b(t_b^{\max})$ in Fig. 3 apparently exceeds $\chi_b^0(t_b^{\max})$ by a few tens of percent. Thus, we cannot draw a definite conclusion on the relation between $\chi_b(t_b^{\max})$ and $\chi_b^0(t_b^{\max})$.

In Fig. 9, we give $\chi_4(t)$ in Eq. (4.14) as a function of t for various T, which is calculated in the NVE ensemble with $N = 4000$. It is maximized at $t = t_4^{\max}$. Here, due to the transverse sound propagation, a smaller acoustic peak emerges with lowering T at $t = t_a/2 \sim 8.6$ [55], whose existence has not been reported in the previous papers. It becomes more evident at lower T, where the acoustic damping is weaker. We also calculated $\chi_4(t)$ for other N. For $N = 64\,000$, the acoustic peak was at $t \sim 34$ and its height even exceeded the first peak height for low T. For $N = 1000$, there was no acoustic peak. [See item (3) in the summary for more discussions.]

Lačević *et al.* [23] determined the overlap length $a\sigma_2$ to maximize the peak height of the four-point susceptibility $\chi_4(t_4^{\max})$ as a function of the parameter a at $T = 0.59$ in 3D. They then obtained $a = 0.3$ and used it also at other low T. Following their method, we also maximized $\chi_4(t_4^{\max})$ as a function of the overlap length to obtain $A_4 = 0.3$ in Eq. (4.3) for $T = 0.64$ and $N = 4000$. Then $t_4^{\max} \sim 10^4$ at $T = 0.56$ both for $N = 4000$ and $64\,000$.

In Fig. 10(a), we plot $S_4(q,t_4^{\max})$ vs q for various T with $N = 64\,000$. In its calculation, we took the average over the initial time t_0 in the wide range $[0,10^6]$. As in the case of $S_b(q,t)$ in Eq. (3.20), we may fit $S_4(q,t)$ to the Ornstein-Zernike form as [23]

$$S_4(q,t) = \chi_4^0(t)/[1 + q^2\xi_4(t)^2], \qquad (4.15)$$

where $\chi_4^0(t) = \lim_{q\to 0} S_4(q,t)$ is the long-wavelength limit of $S_4(q,t)$ and $\xi_4(t)$ is the four-point correlation length. Furthermore, in Fig. 10(b), we show $S_4(q,t_4^{\max})$ at $T = 0.56$ for various N up to $N = 256\,000$ to demonstrate its significant system-size dependence at small q. In Fig. 10(c), we display $\xi_4(t_4^{\max})$ vs T for $N = 64\,000$ as an example, which increases with lowering T. We recognize that the ratio $\xi_4(t_4^{\max})/\xi_b(t_b^{\max})$ exceeds unity and increases with increasing N. For example, it is about 3 for $T = 0.56$ and $N = 64\,000$. Thus, on our 2D simulation, the effect of the low-frequency vibration modes on the four-point correlations becomes stronger for larger N.

V. COMPARISON OF THE TWO THEORETICAL SCHEMES

A. Time scales

In Fig. 11, we display $\phi_b(t)$, $\phi_4(t)$, $\chi_b(t)$, and $\chi_4(t)$ at $T = 0.64$ for $N = 4000$ in the two theoretical schemes. Here, $\phi_b(t)$ is the fraction of the particles with $\mathcal{B}_i > 0$ and $\phi_4(t)$ is that with $\mathcal{F}_i = 0$. We can see that $\phi_b \sim 1/2$ at $t = t_b^{\max}$ and $\phi_4 \sim 1/2$

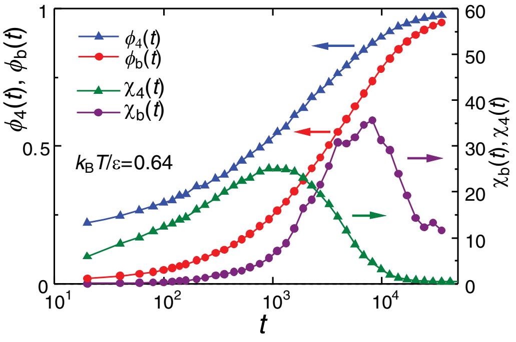

FIG. 11. (Color online) Fraction $\phi_b(t)$ and susceptibility $\chi_b(t)$ for bond breakage and those $\phi_4(t)$ and $\chi_4(t)$ for four-point correlations for $T = 0.64$ and $N = 4000$. Here, $\chi_b(t)$ and $\chi_4(t)$ are maximized for $\phi_b(t) \sim 1/2$ and $\phi_4(t) \sim 1/2$, respectively.

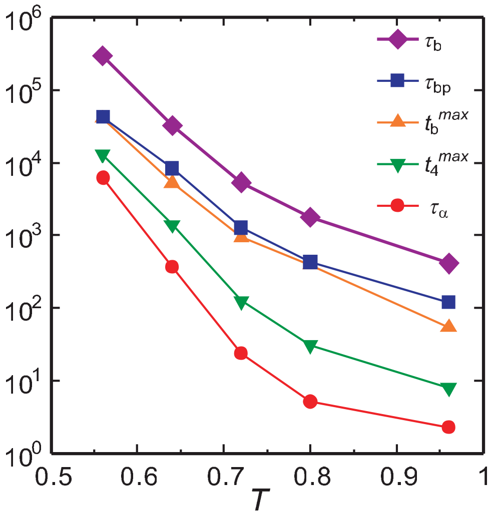

FIG. 12. (Color online) Relaxation times as functions of T for the soft-core potential for $N = 4000$ in 2D. From above, they are τ_b in Eq. (3.4), $\tau_{\rm bp}$ in Eq. (3.16), $t_b^{\rm max}$ from the maximum of $\chi_b(t)$, $t_4^{\rm max}$ from the maximum of $\chi_4(t)$, and τ_α in Eq. (3.6).

at $t = t_4^{\rm max}$. If $\phi_b(t)$ [or $\phi_4(t)$] is close to 0 or 1, $S_b(q,t)$ [or $S_4(q,t)$] becomes very small.

So far we have introduced the bond-breakage time τ_b in Eq. (3.4), the relaxation time τ_α from $F_s(q,t)$ in Eq. (3.6), the bond-preserving time $\tau_{\rm bp}$ in Eq. (3.16), the maximization time $t_b^{\rm max}$ of $\chi_b(t)$ in Fig. 3(a), and the maximization time $t_4^{\rm max}$ of $\chi_4(t)$ in Fig. 9. In Fig. 12, these times are in the following order:

$$\tau_\alpha < t_4^{\rm max} < t_b^{\rm max} \sim \tau_{\rm bp} < \tau_b, \tag{5.1}$$

with $35 \leqslant \tau_b/\tau_\alpha \leqslant 10^2$ in the range $0.56 \leqslant T \leqslant 0.96$ for $N = 4000$. In our 2D simulation, τ_α and $t_4^{\rm max}$ exhibit strong system-size dependence due to the low-frequency vibration modes. In fact, we numerically obtained $\tau_\alpha = 8400$ for $N = 4000$ and $\tau_\alpha = 2140$ for $N = 64\,000$ (see the Appendix). It is worth noting that significant system-size dependence of the plateau behavior of $F_s(q,t)$ [and τ_α from Eq. (3.6)] has been reported in 2D and 3D simulations [27,56,57]. Furthermore, Karmakar *et al.* [27] examined system-size dependence of ξ_4 and $S_4(q,t)$ up to $N = 351\,232$ in 3D.

In addition, we comment on the stress-time-correlation function, which considerably decreases in the early stage due to the thermal motions as well as $F_s(q,t)$. As a result, its relaxation time is of order τ_α [30], while the nonlinear flow behavior is characterized by τ_b [14].

B. Time evolution on long and short time scales

In Fig. 13(a), the arrows represent relatively large displacements $\Delta \boldsymbol{r}_i = \boldsymbol{r}_i(t_1) - \boldsymbol{r}_i(t_0)$ with $\Delta r_i = |\Delta \boldsymbol{r}_i| > 0.3$ [11,17]. We can see both large-amplitude stringlike motions and smaller-amplitude collective motions. In Fig. 13(b), all the $\boldsymbol{B}$ particles are displayed. In Fig. 13(c), those with $\mathcal{F}_i = 0$ are divided into $\boldsymbol{B}$ and non-$\boldsymbol{B}$ particles, where the former exhibit patterns closely resembling those of the $\boldsymbol{B}$ particles in Fig. 13(b). The number of $\boldsymbol{B}$ particles with $\mathcal{F}_i = 0$ is about 70% of that of the total $\boldsymbol{B}$ particles in Fig. 13(b).

From Figs. 13(a) and 13(c), the non-$\boldsymbol{B}$ particles with $\mathcal{F}_i = 0$ mostly arise from the collective motions on large scales, as has been the case at short times in Fig. 7. Their selection is very sensitive to the overlap length, $a\sigma_2$ in the original work [23] and $A_4\sigma_1$ in this paper, while the $\boldsymbol{B}$ particles (even with $\mathcal{F}_i = 0$) are relatively insensitive to it. In the four-point theory [23], the overlap length was chosen to maximize $\chi_4^{\rm max} = \chi_4(t_4^{\rm max})$, as discussed above Eq. (4.15). Roughly speaking, their method is to maximize the contribution from the thermal collective motions of non-$\boldsymbol{B}$ particles to $\chi_4(t)$ (see Fig. 11).

We next examine time evolution at two consecutive times $t = 10\,200$ and $10\,400$ for $N = 4000$ (left) and $64\,000$ (right) at $T = 0.56$. The four upper panels of Fig. 14 display the particles with $\mathcal{F}_i(t_0,t_0+t) = 0$ grouped into $\boldsymbol{B}$ and non-$\boldsymbol{B}$ particles. These snapshots are subsequent to that in Fig. 13(c) for $N = 4000$ and that in the box region in Fig. 8 for $N = 64\,000$ in the same runs. The four lower panels of Fig. 14 give the corresponding displacements $\Delta \boldsymbol{r}_i(t_0+t', t_0+t'+200)$ with $t' = 100\,00$ or $10\,200$, which exceed 0.3 in this short time interval of 200. The differences between the consecutive patterns are evidently larger for $N = 64\,000$ than for $N = 4000$. We can see that this system-size dependence originates from the large-scale vibrational motions.

In Table I, we give the numbers of the particles with (a) $\mathcal{B}_i > 0$, (b) $\mathcal{B}_i > 0$ and $\mathcal{F}_i = 0$, (c) $\mathcal{B}_i = \mathcal{F}_i = 0$, and (d) $\Delta r_i > 0.3$

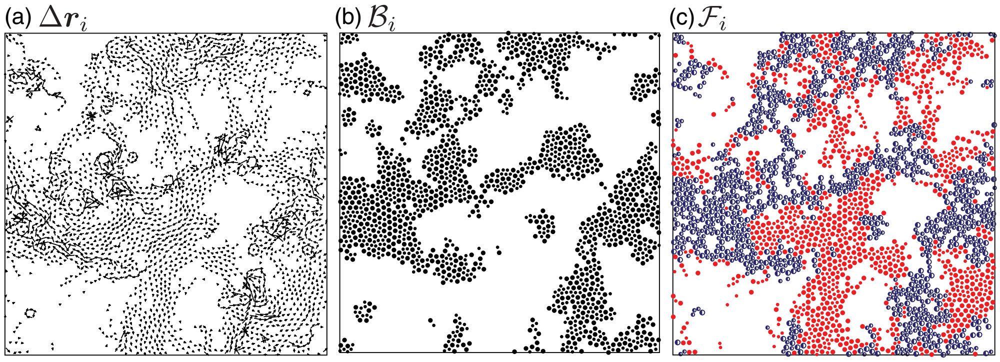

FIG. 13. (Color online) Snapshots at $t = t_1 - t_0 = 10^4$ for $T = 0.56$ and $N = 4000$ in 2D. System length is $L = 70.2$. (a) Displacements $\Delta \boldsymbol{r}_i(t_0,t_1)$ with $|\Delta \boldsymbol{r}_i| > 0.3$, (b) $\boldsymbol{B}$ particles, and (c) those with $\mathcal{F}_i = 0$ classified into $\boldsymbol{B}$ particles (crescentic symbol in blue) and non-$\boldsymbol{B}$ particles (full circle symbol in red). Non-$\boldsymbol{B}$ particles with $\mathcal{F}_i = 0$ are produced by collective motions, while most $\boldsymbol{B}$ particles participate in stringlike motions and satisfy $\mathcal{F}_i = 0$.

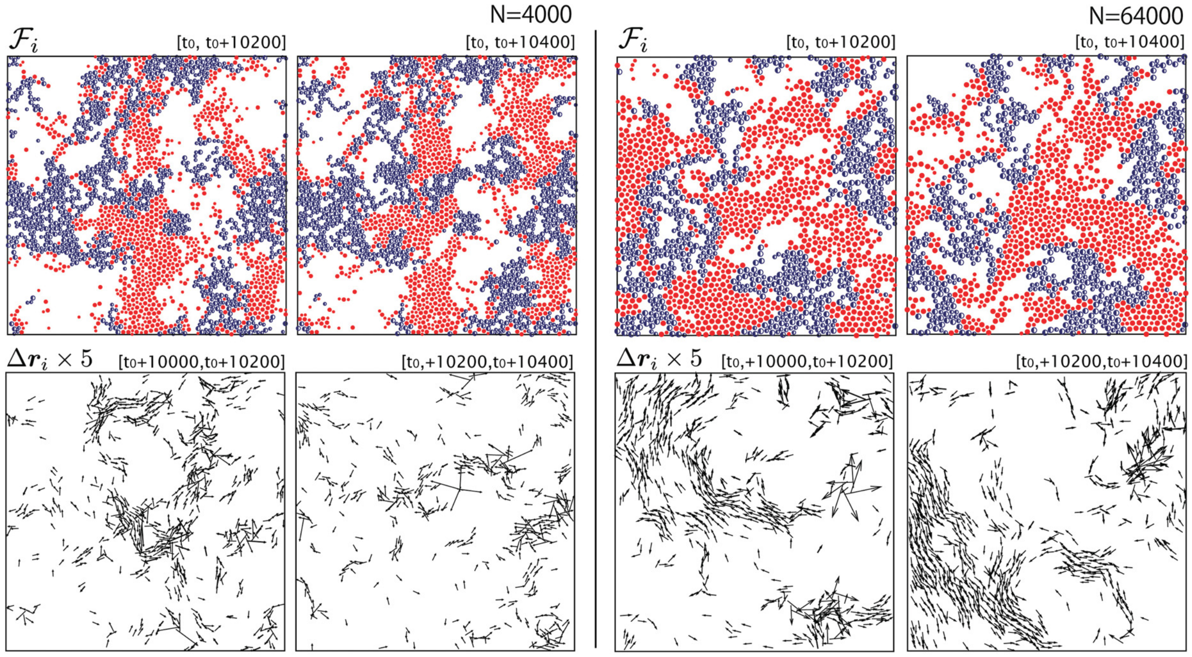

FIG. 14. (Color online) Snapshots at $t = 10\,000 + 200k$ ($k = 1,2$) at $T = 0.56$ for $N = 4000$ (left) and for $N = 64\,000$ (right). Top: Particles with $\mathcal{F}_i = 0$ classified into non-$\boldsymbol{B}$ particles (full circle symbol in red) and $\boldsymbol{B}$ particles (crescentic symbol in blue), where the former significantly change but the latter little change in this short time interval. The change of the former is larger for the larger N in the right. See the preceding snapshots in (c) of Fig. 13 for $N = 4000$ and in the black box of Fig. 8 for $N = 64\,000$. Bottom: Displacements $\Delta\boldsymbol{r}_i = \Delta\boldsymbol{r}_i(t_0 + t', t_0 + t' + 200)$ multiplied by 5 with $|\Delta\boldsymbol{r}_i| > 0.3$ in short time intervals of 200, where $t' = 10\,000$ or $10\,200$.

in the four snapshots in Fig. 14. We also give those of the particles commonly depicted in the consecutive snapshots. In Table II, the numbers of the $\boldsymbol{B}$ and non-$\boldsymbol{B}$ particles are given at $t = 10\,200$ for (a) $\Delta r_i > 0.3$ and $\mathcal{F}_i = 0$, (b) $\Delta r_i > 0.3$ and $\mathcal{F}_i = 1$, and (c) $\Delta r_i < 0.3$ and $\mathcal{F}_i = 1$. There is no particle with $\Delta r_i < 0.3$ and $\mathcal{F}_i = 0$. We recognize the following: (i) About 20%–30% of the particles with $\mathcal{F}_i = 0$ change into those with $\mathcal{F}_i = 1$ and vice versa in a short time of 200. (ii) About 30% of the $\boldsymbol{B}$ particles satisfy $\mathcal{F}_i = 1$ at each time because of the presence of another particle j within their initial circles. As stated at the end of Sec. IV A, most of the particles with $\Delta r_i > 0.3$ and $\mathcal{F}_i = 1$ are $\boldsymbol{B}$ particles having broken bonds (which is 97% in the example of Table II). (iii) About 5% of the $\boldsymbol{B}$ particles become the non-$\boldsymbol{B}$ particles and vice versa in a short time of 200. (iv) About 85% of the $\boldsymbol{B}$ particles move outside their initial circle to have $\Delta r_i > 0.3$. The remaining 15% of the $\boldsymbol{B}$ particles stay within their initial circle having broken bonds after long-distance motions of the neighboring particles.

TABLE I. Particle numbers with (a) $\mathcal{B}_i > 0$, (b) $\mathcal{B}_i > 0$ and $\mathcal{F}_i = 0$, (c) $\mathcal{B}_i = \mathcal{F}_i = 0$, and (d) $\Delta r_i > 0.3$ in Fig. 14 at $t = 10\,200$ and 10 400 for $N = 4000$ and 64 000 in 2D. Those of the particles common in these two shots are also given. Subscript i is omitted from Δr_i, $\mathcal{B}_i$, and $\mathcal{F}_i$.

t (N)	$\mathcal{B} > 0$	$\mathcal{B} > 0, \mathcal{F} = 0$	$\mathcal{B} = \mathcal{F} = 0$	$\Delta r > 0.3$
10200 (4000)	1629	1104	1091	2451
10400 (4000)	1667	1180	1221	2643
Common (4000)	1576	925	823	1923
10200 (64000)	26 188	18 336	20 884	43 544
10400 (64000)	26 413	18 678	21 785	44 693
Common (64000)	25 192	14 149	14 349	31 790

Dauchot *et al.* [58] performed an experiment on a 2D dense granular packing under cyclic shear near the jamming transition. Their snapshots of $\Delta\boldsymbol{r}_i$ and $1 - \mathcal{F}_i$ ($\hat{q}_s^a$ in their notation) resemble those in Fig. 13.

VI. THREE-DIMENSIONAL RESULTS

Also in 3D, the four-point correlations arise from the bond-breakage motions and the thermal vibrational motions. The former grow slowly with structural relaxations, while the latter fluctuate relatively rapidly.

In Fig. 15, we give snapshots of the particles at $t = 10\,000$ and 10 200 for $T = 0.24$ and $N = 10^4$, where $\tau_\alpha \sim 10^5$. The system length is $L = 23.2$. Here, the fraction of the $\boldsymbol{B}$ particles is $\phi_B(t) \sim 0.24$ and that with $\mathcal{F}_i = 0$ is $\phi_4(t) \sim 0.15$. In Fig. 15(a), we display the relatively large displacements $\Delta\boldsymbol{r}_i = \boldsymbol{r}_i(t_0 + t) - \boldsymbol{r}_i(t_0)$ with $\Delta r_i > 0.3$. Stringlike motions are conspicuous [14,15,23,33], around which collective motions

TABLE II. Numbers of non-$\boldsymbol{B}$ and $\boldsymbol{B}$ particles for three categories in Fig. 14 at $t = 10\,200$ for $N = 4000$ in 2D.

	$\Delta r > 0.3$ $\mathcal{F} = 0$	$\Delta r > 0.3$ $\mathcal{F} = 1$	$\Delta r < 0.3$ $\mathcal{F} = 1$	Total
$\mathcal{B} = 0$	1091	7	1273	2371
$\mathcal{B} > 0$	1104	249	276	1629
Total	2195	256	1549	4000

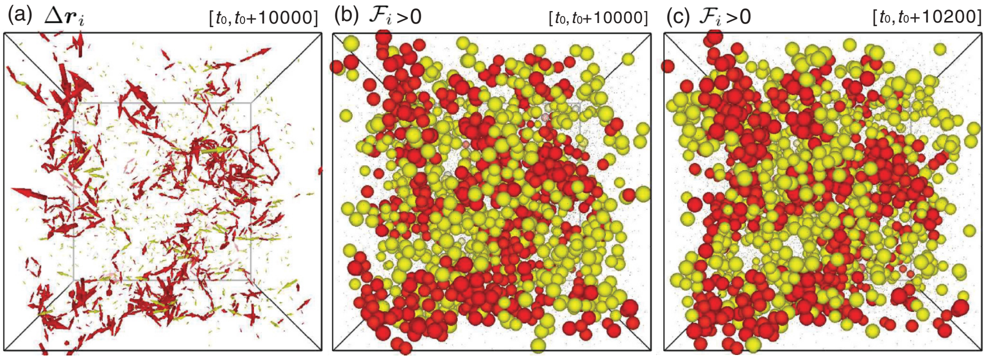

FIG. 15. (Color online) Snapshots in 3D for $T = 0.24$ and $N = 10\,000$. (a) Arrows indicate displacements $\Delta \boldsymbol{r}_i(t_0,t_0 + 10\,000)$ with $|\Delta \boldsymbol{r}_i| > 0.3$, whose number is 1818. Particles with $\mathcal{F}_i = 0$ classified into $\boldsymbol{B}$ particles (red or dark) and non-$\boldsymbol{B}$ particles (yellow or bright) for time intervals $[t_0,t_0 + 10\,000]$ in (b) and $[t_0,t_0 + 10\,200]$ in (c). Depicted non-$\boldsymbol{B}$ particles are produced by the vibration modes and are fluctuatiing in time, while $\boldsymbol{B}$ particles are not much changed between these two times.

with $\Delta r_i > 0.3$ tend to be induced. We also display the particles with $\mathcal{F}_i = 0$ grouping them into $\boldsymbol{B}$ particles (in red or dark gray) and non-$\boldsymbol{B}$ particles (in yellow or bright gray) in time intervals $[t_0,t_0 + 10\,000]$ in Fig. 15(b) and $[t_0,t_0 + 10\,200]$ in Fig. 15(c).

In Fig. 16, we display the $\boldsymbol{B}$ particles in (a) and (a′), the $\boldsymbol{B}$ particles with $\mathcal{F}_i = 0$ in (b) and (b′), and the non-$\boldsymbol{B}$ particles with $\mathcal{F}_i = 0$ in (c) and (c′) for $t = 10\,000$ in the left and 10 200 in the right. We use the same data as in Fig. 15. We can see that the $\boldsymbol{B}$ particles little change, but the non-$\boldsymbol{B}$ particles greatly change in a time interval of 200. The aggregates of the $\boldsymbol{B}$ particles have grown from the strings in Fig. 15(a). The number of the total $\boldsymbol{B}$ particles (in the top panels) is considerably larger than that of the $\boldsymbol{B}$ particles with $\mathcal{F}_i = 0$ (in the middle panels), which are 2351 and 641, respectively, at $t = 10\,000$. This is because the particles surrounding each string can have broken bonds without their long-disance motions.

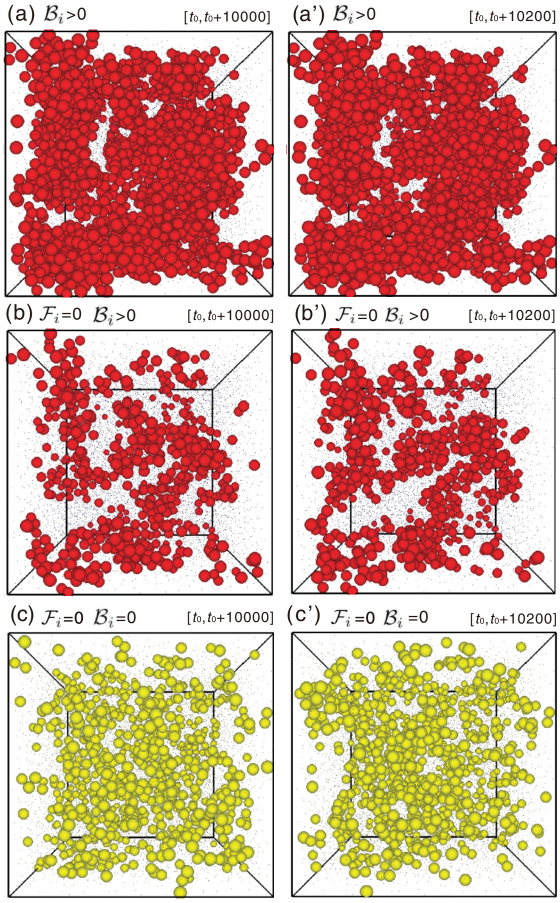

FIG. 16. (Color online) Snapshots using the data in Fig. 15 for time intervals $[t_0,t_0 + 10\,000]$ (left) and $[t_0,t_0 + 10\,200]$ (right). Displayed are particles with $\mathcal{B}_i > 0$ in (a), those with $\mathcal{B}_i > 0$ and $\mathcal{F}_i = 0$ in (b), and those with $\mathcal{B}_i = \mathcal{F}_i = 0$ in (c).

Table III gives the numbers of the particles with (a) $\mathcal{B}_i > 0$, (b) $\mathcal{B}_i > 0$ and $\mathcal{F}_i = 0$, (c) $\mathcal{B}_i = \mathcal{F}_i = 0$, and (d) $\Delta r_i > 0.3$ in the two snapshots in Figs. 15 and 16. Also given in the last line are those of the particles commonly depicted in the consecutive snapshots. On the other hand, Table IV presents the numbers of the $\boldsymbol{B}$ and non-$\boldsymbol{B}$ particles at $t = 10\,200$ for (a) $\Delta r_i > 0.3$ and $\mathcal{F}_i = 0$, (b) $\Delta r_i > 0.3$ and $\mathcal{F}_i = 1$, and (c) $\Delta r_i < 0.3$ and $\mathcal{F}_i = 1$. Conspicuous features are as follows: (i) About 50% of the particles with $\Delta r_i > 0.3$ change into those with $\Delta r_i < 0.3$ and vice versa in a short time interval of 200. Only 30% of the non-$\boldsymbol{B}$ particles are common in the two consecutive snapshots. (ii) About 60% of the $\boldsymbol{B}$ particles satisfy $\Delta r_i < 0.3$ and $\mathcal{F}_i = 0$. (The corresponding percentage is about 15% in 2D in Table II.) This is because of the larger coordination number or the larger bonded particles around each particle in 3D. That is, there are about ten bonded particles around a particle which has participated in a stringlike motion and moved over a molecular distance. (iii) The particles with $\Delta r_i > 0.3$ and $\mathcal{F}_i = 1$ amount to 366 and their fraction in those with $\Delta r_i > 0.3$ is about 0.2. This means that the distinct part is negligible as compared to the self part in $\mathcal{F}_i$ in Eq. (4.2), in accord with the calculation by Lačević *et al.* [23]. (iv) Among

TABLE III. Particle numbers in Figs. 15 and 16 at $t = 10\,000$ and 10 200 for $N = 10^4$ in 3D.

t	$\mathcal{B} > 0$	$\mathcal{B} > 0, \mathcal{F} = 0$	$\mathcal{B} = \mathcal{F} = 0$	$\Delta r > 0.3$
10 000	2351	641	811	1818
10 200	2393	675	898	1943
Common	2094	400	268	980

TABLE IV. Numbers of non-$\boldsymbol{B}$ and $\boldsymbol{B}$ particles for three categories at $t = 10\,000$ for $N = 10^4$ in 3D in Figs. 15 and 16.

	$\Delta r > 0.3$ $\mathcal{F} = 0$	$\Delta r > 0.3$ $\mathcal{F} = 1$	$\Delta r < 0.3$ $\mathcal{F} = 1$	Total
$\mathcal{B} = 0$	811	27	6811	7649
$\mathcal{B} > 0$	641	339	1371	2351
Total	1452	366	8182	10 000

366 particles with $\Delta r_i > 0.3$ and $\mathcal{F}_i = 1$, most of them (339) are $\boldsymbol{B}$ particles.

VII. SUMMARY AND REMARKS

We have examined the dynamic heterogeneity of glassy particle systems in the bond-breakage scheme [13,14] and in the four-point scheme [23]. The former treats the irreversible configuration changes, while in the latter also included are the reversible particle displacements due to the low-frequency vibrational modes. These two kinds of motions are both highly heterogeneous in glassy states.

Our main results are as follows:

(i) In Sec. III, we have generalized the bond-breakage theory [13,14] to define the broken bond number $\mathcal{B}_i(t_0,t_1)$, the fractions of the particles with k broken bonds $\phi_b(t,k)$, the correlation function $G_b(r,t)$, the structure factor $S_b(q,t)$, and the susceptibility $\chi_b(t)$ in Eqs. (3.12), (3.14), and (3.19)–(3.21). We have defined the bond-breakage time τ_b in Eq. (3.4) and the bond-preserving time $\tau_{\rm bp}$ in Eq. (3.16) in addition to the relaxation time τ_α from $F_s(q,t)$ in Eq. (3.6). In Fig. 3, $\chi_b(t)$ exhibits a maximum as a function of t, yielding the maximization time $t_b^{\rm max}$, while the Ornstein-Zernike fitting of $S_b(q,t_b^{\rm max})$ yields $\xi_b = \xi_b(t_b^{\rm max})$ in Fig. 4. These quantities are nearly independent of the system size as long as $1 \ll \xi_b \ll L$.

(ii) In Sec. IV, we have discussed the four-point theory, where the overlap function $w(r)$ in Eq. (4.3) defines the initial circles (spheres) in 2D (3D). The overlap number $\mathcal{F}_i(t_0,t_1)$ in Eq. (4.2) determines the correlation function $G_4(r,t)$, the structure factor $S_4(q,t)$, and the susceptibility $\chi_4(t)$ in Eqs. (4.12)–(4.14). Maximization of $\chi_4(t)$ with respect to t yields the characteristic time $t_4^{\rm max}$. We have shown that the nonoverlap motions from the initial circles stem from the thermal excitation of the low-frequency vibrational modes and the escape jumps from temporary cages as in Figs. 5, 6, 11, and 13. The thermal collective motions appear from the initial stage ($t \gtrsim 10$) as in Fig. 7, while the jump motions emerge very slowly. The maximization procedure of $\chi_4(t)$ with respect to the overlap length [23] is to maximize the contribution from the thermal collective motions to $\chi_4(t)$. In 2D, the system-size dependence of the four-point correlations is strong at long wavelengths even for $\xi_4 \ll L$.

(iii) In Sec. V, we have compared the relaxation times τ_b, τ_{pb}, τ_α, $t_b^{\rm max}$, and $t_4^{\rm max}$ in Fig. 12 to obtain the sequence (5.1), where $\tau_\alpha(\sim t_4^{\rm max})$ is considerably shorter than τ_b. Next we have presented snapshots of the displacements $\mathcal{B}_i$, and $\mathcal{F}_i$ at $t = 10^4$ for $N = 4000$ with marked large-scale heterogeneities in Fig. 13. We have grouped the particles with $\mathcal{F}_i = 0$ into $\boldsymbol{B}$ and non-$\boldsymbol{B}$ particles, where they are those with and without broken bonds, respectively. The patterns of the $\boldsymbol{B}$ particles with $\mathcal{F}_i = 0$ closely resemble those of the total $\boldsymbol{B}$ particles. The non-$\boldsymbol{B}$ particles with $\mathcal{F}_i = 0$ arise from the low-frequency vibration modes undergoing relatively rapid temporal variations, as can be seen in the inset of Fig. 5 and in Fig. 14.

(iv) Also in 3D, the four-point correlations arise from the thermal collective motions with $\mathcal{B}_i = 0$ and the bond-breakage motions with $\mathcal{B}_i \geqslant 1$ as in Figs. 15 and 16. As a characteristic feature in 3D, Table IV shows that about 60% of the $\boldsymbol{B}$ particles satisfy $\Delta r_i < 0.3$ and $\mathcal{F}_i = 1$. These particles surround the particles which have undergone stringlike motions.

We make some remarks in the following.

(1) The heterogeneity exhibited by the low-frequency vibration modes still remains largely unexplored [35–41]. In future work, we should examine how it depends on the size ratio and the composition [45–47].

(2) The vibration modes determine the plateaus of the time-correlation function $F_s(q,t)$ in Eq. (3.5) and the mean square displacement $M(t)$ in Eq. (A4), resulting in significant system-size effects [56,57]. They also give rise to the system-size dependence of the four-point structure $S_4(q,t)$ at small q in Fig. 10(b). Our present analysis is mostly for 2D, but Eqs. (A2) and (A8) provide one possible source of the finite size effect in 3D.

(3) We also comment on the effect of a thermostat, which was used only in preparing the initial states. We have found that a thermostat can strongly affect the low-frequency vibration modes (not shown in this paper). For example, the second peak of $\chi_4(t)$ at $t \cong L/2c_\perp$ for $T \leqslant 0.80$ in Fig. 9 disappeared in the presence of a thermostat, presumably because it effectively increases the acoustic damping.

ACKNOWLEDGMENTS

This work was supported by Grant-in-Aid for Scientific Research from the Ministry of Education, Culture, Sports, Science and Technology of Japan. T.K. was supported by the Japan Society for Promotion of Science. The authors would like to thank Ryoichi Yamamoto, Kunimasa Miyazaki, Shin-ichi Sasa, and Kang Kim for informative discussions. The numerical calculations were carried out on SR16000 at YITP in Kyoto University and Altix ICE 8400EX at ISSP in University of Tokyo.

APPENDIX: THERMAL POSITIONAL FLUCTUATIONS AND FINITE SIZE EFFECT

In solids, the vibration modes give rise to the thermal fluctuations of the particle displacements $\boldsymbol{u}_i(t) = \boldsymbol{r}_i(t) - \bar{\boldsymbol{r}}_i$ with $\bar{\boldsymbol{r}}_i$ being the time-averaged positions. In our theory, we may define $\bar{\boldsymbol{r}}_i$ on time scales shorter than the bond-preserving time $\tau_{\rm bp}$ in Eq. (3.16). The contributions from the large-scale modes may be calculated using the classical linear elasticity theory, which should be valid at sufficiently long wavelengths even in glass [35].

In 2D, we may express the displacement variance $\langle |\boldsymbol{u}|^2\rangle = \sum_i \langle |\boldsymbol{u}_i|^2\rangle/N$ as in Eqs. (4.6) and (4.7). For 2D solids [54], use has been made of the relation

$$\langle |\boldsymbol{u}_i(t) - \boldsymbol{u}_j(t)|^2\rangle = 2C_1 \ln(r_{ij}/a_0), \tag{A1}$$

where C_1 is given in Eq. (4.7), r_{ij} is the distance between particles i and j, and a_0 is a microscopic length. Thus, Eq. (A1) represents the anomalous long-range correlation in 2D solids. These expressions follow if the discrete sums over the long-wavelength vibration modes ($\sum_{\boldsymbol{q}} |\boldsymbol{q}|^{-2}$) are replaced by the wave-number integral ($\int dq\, q^{d-3}$). In 3D, there is no long-wavelength divergence, but the lower bound of the wave number ($\propto L^{-1}$) yields the following L dependence:

$$\langle |\boldsymbol{u}|^2 \rangle = D_0 - D_1/L, \tag{A2}$$

where D_0 and D_1 are functions of T. If we perform the corresponding discrete summation over the modes under the periodic boundary condition, we obtain

$$D_1 = 0.21 k_B T \left(\frac{2}{\mu} + \frac{1}{K + 4\mu/3} \right). \tag{A3}$$

For $t \ll \tau_{\rm bp}$, we may set $\boldsymbol{r}_i(t_0) - \boldsymbol{r}_i(t_0 + t) = \boldsymbol{u}_i(t_0) - \boldsymbol{u}_i(t_0 + t)$ by neglecting the configuration changes. The mean square displacement $M(t)$ is written as

$$\begin{aligned} M(t) &= \sum_i \langle |\boldsymbol{r}_i(t_0) - \boldsymbol{r}_i(t_0 + t)|^2 \rangle / N \\ &\cong \sum_i \langle |\boldsymbol{u}_i(t_0) - \boldsymbol{u}_i(t_0 + t)|^2 \rangle / N. \end{aligned} \tag{A4}$$

If the cross correlation $\sum_i \langle \boldsymbol{u}_i(t_0 + t) \cdot \boldsymbol{u}_i(t_0) \rangle / N$ decays to zero due to the acoustic damping before the α relaxation, a well-defined plateau $M_{\rm p}$ appears in $M(t)$ with

$$M(t) \cong M_{\rm p} = 2\langle |\boldsymbol{u}|^2 \rangle, \tag{A5}$$

for $1 \ll t \ll \tau_{\rm bp}$ as already given in Eq. (4.6).

The time correlation function $F_s(q,t)$ in Eq. (3.5) also assumes a well-defined plateau value $f_{\rm p} = f_{\rm p}(T,N)$ at low T. For the Gaussian distribution of $\boldsymbol{u}_i$, we have [59]

$$f_{\rm p} \cong \exp[-q^2 M_{\rm p}/2d] = \exp[-q^2 \langle |\boldsymbol{u}|^2 \rangle / d]. \tag{A6}$$

If the structural relaxation time τ_α is defined by Eq. (3.6), its dependence on $N (\propto N^{1/d})$ can arise from Eq. (4.6) in 2D and from Eq. (A2) in 3D.

For 2D, $f_{\rm p}$ depends on N as

$$f_{\rm p} \propto L^{-q^2 C_1/2} \propto N^{-q^2 C_1/4}. \tag{A7}$$

For $T = 0.56$ and $q = 2\pi$, our numerical analysis gives $f_{\rm p} = 0.6$ for $N = 4000$ in Fig. 1 and $f_{\rm p} = 0.5$ for $N = 64\,000$. The ratio of these two values $0.6/0.5 = 1.2$ is close to the theoretical ratio $16^{q^2 C_1/4} = 1.17$ from Eq. (A7).

For 3D, Eqs. (A2), (A5), and (A6) yield

$$f_{\rm p}(T,N)/f_{\rm p}(T,\infty) = \exp[B_f N^{-1/3}]. \tag{A8}$$

Under the periodic boundary condition, Eq. (A3) gives

$$B_f \cong 0.14 q^2 k_B T n^{1/3}/\mu, \tag{A9}$$

where K is assumed to be considerably larger than μ. Kim and Yamamoto [57] studied the finite size effect using the soft-core potential for $N = 108, 10^3$, and 10^4 in 3D. Their data of $F_s(q,t)$ at $t = 10$ for $q = 2\pi$ and $T = 0.267$ may be approximately fitted to the form $\propto \exp[0.25 N^{-1/3}]$, while Eqs. (A8) and (A9) give $f_{\rm p} \propto \exp[0.29 N^{-1/3}]$ (where we obtain $\mu = 5$ from the stress-strain relation).

---

[1] K. Binder and W. Kob, *Glassy Materials and Disordered Solids* (World Scientific, Singapore, 2005).

[2] G. Adam and J. H. Gibbs, J. Chem. Phys. **43**, 139 (1965).

[3] H. Sillescu, J. Non-Cryst. Solids **243**, 81 (1999).

[4] M. D. Ediger, Annu. Rev. Phys. Chem. **51**, 99 (2000).

[5] L. Berthier, G. Biroli, J.-P. Bouchaud, L. Cipelletti, and W. van Saarloos, *Dynamical Heterogeneities in Glasses, Colloids, and Granular Media* (Oxford University Press, Oxford, 2011).

[6] K. Maeda and S. Takeuchi, Phys. Status Solidi A **44**, 685 (1978); Philos. Mag. A **44**, 643 (1981).

[7] D. Srolovitz, V. Vitek, and T. Egami, Acta. Metall. **31**, 335 (1983).

[8] D. Deng, A. S. Argon, and S. Yip, Philos. Trans. R. Soc. London, Ser. A **329**, 595 (1989); **329**, 613 (1989).

[9] M. M. Hurley and P. Harrowell, Phys. Rev. E **52**, 1694 (1995).

[10] D. N. Perera and P. Harrowell, Phys. Rev. Lett. **81**, 120 (1998); J. Chem. Phys. **111**, 5441 (1999).

[11] T. Muranaka and Y. Hiwatari, Phys. Rev. E **51**, R2735 (1995).

[12] Y. Hiwatari and T. Muranaka, J. Non-Cryst. Solids **235–237**, 19 (1998). Figure 6 of their paper is similar to Fig. 7(a) in the present paper.

[13] R. Yamamoto and A. Onuki, J. Phys. Soc. Jpn. **66**, 2545 (1997).

[14] R. Yamamoto and A. Onuki, Phys. Rev. E **58**, 3515 (1998). See Fig. 16 of this paper for the relation between τ_b and τ_α; J. Phys.: Condens. Matter **29**, 6323 (2000).

[15] W. Kob, C. Donati, S. J. Plimpton, P. H. Poole, and S. C. Glotzer, Phys. Rev. Lett. **79**, 2827 (1997); C. Donati, J. F. Douglas, W. Kob, S. J. Plimpton, P. H. Poole, and S. C. Glotzer, *ibid.* **80**, 2338 (1998); C. Donati, S. C. Glotzer, P. H. Poole, W. Kob, and S. J. Plimpton, Phys. Rev. E **60**, 3107 (1999).

[16] D. N. Perera, J. Phys.: Condens. Matter **10**, 10115 (1998).

[17] B. Doliwa and A. Heuer, Phys. Rev. E **61**, 6898 (2000); J. Non-Cryst. Solids **307–310**, 32 (2002).

[18] D. Chandler, J. P. Garrahan, R. L. Jack, L. Maibaum, and A. C. Pan, Phys. Rev. E **74**, 051501 (2006).

[19] G. Biroli, J.-P. Bouchaud, K. Miyazaki, and D. R. Reichman, Phys. Rev. Lett. **97**, 195701 (2006).

[20] R. Candelier, A. Widmer-Cooper, J. K. Kummerfeld, O. Dauchot, G. Biroli, P. Harrowell, and D. R. Reichman, Phys. Rev. Lett. **105**, 135702 (2010).

[21] T. Kawasaki, T. Araki, and H. Tanaka, Phys. Rev. Lett. **99**, 215701 (2007).

[22] R. Yamamoto and A. Onuki, Phys. Rev. Lett. **81**, 4915 (1998).

[23] N. Lačević, F. W. Starr, T. B. Schroder, and S. C. Glotzer, J. Chem. Phys. **119**, 7372 (2003).

[24] L. Berthier, G. Biroli, J.-P. Bouchaud, L. Cipelletti, D. E. Masri, D. L'Hôte, F. Ladieu, and M. Pierno, Science **310**, 1797 (2005).

[25] L. Berthier, G. Biroli, J.-P. Bouchaud, W. Kob, K. Miyazaki, and D. R. Reichman, J. Chem. Phys. **126**, 184503 (2007); **126**, 184504 (2007).

[26] D. Chandler, J. P. Garrahan, R. L. Jack, L. Maibaum, and A. C. Pan, Phys. Rev. E **74**, 051501 (2006).

[27] S. Karmakar, C. Dasgupta, and S. Sastry, Phys. Rev. Lett. **105**, 015701 (2010); **105**, 019801 (2010).

[28] E. Flenner, M. Zhang, and G. Szamel, Phys. Rev. E **83**, 051501 (2011).
[29] H. Mizuno and R. Yamamoto, Phys. Rev. E **84**, 011506 (2011).
[30] A. Furukawa and H. Tanaka, Phys. Rev. E **84**, 061503 (2011).
[31] H. R. Schober and B. B. Laird, Phys. Rev. B **44**, 6746 (1991).
[32] W. Schirmacher, G. Diezemann, and C. Ganter, Phys. Rev. Lett. **81**, 136 (1998).
[33] H. R. Schober, C. Oligschleger, and B. B. Laird, J. Non-Cryst. Solids **156–158**, 965 (1993); C. Oligschleger and H. R. Schober, Phys. Rev. B **59**, 811 (1999).
[34] L. Angelani, M. Montagna, G. Ruocco, and G. Viliani, Phys. Rev. Lett. **84**, 4874 (2000).
[35] A. Tanguy, J. P. Wittmer, F. Leonforte, and J.-L. Barrat, Phys. Rev. B **66**, 174205 (2002); F. Leonforte, R. Boissiere, A. Tanguy, J. P. Wittmer, and J.-L. Barrat, *ibid.* **72**, 224206 (2005); F. Leonforte, A. Tanguy, J. P. Wittmer, and J.-L. Barrat, Phys. Rev. Lett. **97**, 055501 (2006).
[36] H. R. Schober and G. Ruocco, Philos. Mag. **84**, 1361 (2004).
[37] H. Shintani and H. Tanaka, Nature Mater. **7**, 870 (2008).
[38] C. Brito and M. Wyart, J. Chem. Phys. **131**, 024504 (2009).
[39] A. Widmer-Cooper, H. Perry, P. Harrowell, and D. R. Reichman, Nature Phys. **4**, 711 (2008); J. Chem. Phys. **131**, 194508 (2009).
[40] A. Ghosh, V. K. Chikkadi, P. Schall, J. Kurchan, and D. Bonn, Phys. Rev. Lett. **104**, 248305 (2010).
[41] K. Chen, W. G. Ellenbroek, Z. Zhang, D. T. N. Chen, P. J. Yunker, S. Henkes, C. Brito, O. Dauchot, W. van Saarloos, A. J. Liu, and A. G. Yodh, Phys. Rev. Lett. **105**, 025501 (2010).
[42] K. Chen, M. L. Manning, P. J. Yunker, W. G. Ellenbroek, Z. Zhang, A. J. Liu, and A. G. Yodh, Phys. Rev. Lett. **107**, 108301 (2011).
[43] K. Vollmayr-Lee, W. Kob, K. Binder, and A. Zippelius, J. Chem. Phys. **116**, 5158 (2002).
[44] A. Widmer-Cooper and P. Harrowell, Phys. Rev. Lett. **96**, 185701 (2006).
[45] T. Hamanaka and A. Onuki, Phys. Rev. E **74**, 011506 (2006); **75**, 041503 (2007).
[46] H. Zhang, D. J. Srolovitz, J. F. Douglas, and J. A. Warren, Phys. Rev. B **74**, 115404 (2006); Proc. Natl. Acad. Sci. USA **106**, 7735 (2009).
[47] H. Shiba and A. Onuki, Phys. Rev. E **81**, 051501 (2010).
[48] M. Tsamados, A. Tanguy, C. Goldenberg, and J.-L. Barrat, Phys. Rev. E **80**, 026112 (2009).
[49] K. Yoshimoto, T. S. Jain, K. Van Workum, P. F. Nealey, and J. J. de Pablo, Phys. Rev. Lett. **93**, 175501 (2004).
[50] Y. Shi, M. B. Katz, H. Li, and M. L. Falk, Phys. Rev. Lett. **98**, 185505 (2007); A. Lemaitre and C. Caroli, Phys. Rev. E **76**, 036104 (2007); A. Furukawa, K. Kim, S. Saito, and H. Tanaka, Phys. Rev. Lett. **102**, 016001 (2009).
[51] M. L. Manning and A. J. Liu, Phys. Rev. Lett. **107**, 108302 (2011).
[52] E. Rabani, J. D. Gezelter, and B. J. Berne, J. Chem. Phys. **107**, 6867 (1997); Phys. Rev. Lett. **82**, 3649 (1999).
[53] A. R. Abate and D. J. Durian, Phys. Rev. E **74**, 031308 (2006).
[54] B. Jancovici, Phys. Rev. Lett. **19**, 20 (1967); Y. Imry and L. Gunther, Phys. Rev. B **3**, 3939 (1971); D. R. Nelson and B. I. Halperin, *ibid.* **19**, 2457 (1979).
[55] In our simulation, the transverse and longitudinal sound velocities are given by $c_\perp = (\mu/\rho)^{1/2} \cong 4.1$ and $c_\parallel = [(K+\mu)/\rho]^{1/2} \cong 8.9$ in units of σ_1/τ_0 at $T = 0.56$ in 2D, where $\rho = 1.06 m_1 \sigma_1^{-2}$ is the average mass density.
[56] T. Muranaka and Y. Hiwatari, Mol. Simul. **16**, 387 (1996); J. Horbach, W. Kob, K. Binder, and C. A. Angell, Phys. Rev. E **54**, R5897 (1996).
[57] K. Kim and R. Yamamoto, Phys. Rev. E **61**, R41 (2000).
[58] O. Dauchot, G. Marty, and G. Biroli, Phys. Rev. Lett. **95**, 265701 (2005).
[59] G. Pastore, B. Bernu, J. P. Hansen, and Y. Hiwatari, Phys. Rev. A **38**, 454 (1988).